DEVELOPMENT OF A 1000W ORGANIC RANKINE CYCLE MICRO-TURBINE-GENERATOR USING POLYMERIC STRUCTURAL MATERIALS AND ITS PERFORMANCE TEST WITH COMPRESSED AIR

Isaias Hernandez-Carrillo [a], Christopher Wood [a], Hao Liu [a1]

[a] Department of Architecture and Built Environment, Faculty of Engineering, University of Nottingham, University Park, Nottingham NG7 2RD, UK

Isaias.HernandezCarrillo@nottingham.ac.uk

Christopher.Wood@nottingham.ac.uk

liu.hao@nottingham.ac.uk

HIGHLIGHTS

- Development of a 1,000 W micro-turbine for an organic Rankine cycle
- Polymeric materials used as the functional parts of the micro-turbine
- Achieved steady rotational speed of 32,000rpm and peak speed of 40,000rpm
- Aerodynamic efficiency predicted to be up to 0.66

ABSTRACT

This paper presents the experimental advances on the implementation of structural polymeric materials in a micro-turbine-generator for an organic Rankine cycle (ORC) and through testing provides an insight of its performance. The aim is to create awareness of the huge techno-economical potential that polymers represent as metal replacement in ORC applications. A micro-turbine-generator is developed considering R245fa as the working fluid. The unit is built using polymeric components; these components include an impeller made from polyether-ether-ketone and a nozzle body made from polyethylene. A program for the simulation of the micro-turbine performance is developed, a series of tests are conducted with compressed air and the performance with R245fa is predicted. The impeller was experimentally demonstrated to be able to withstand a rotational speed of

[1] Corresponding author

32,040rpm whereas the predicted results showed the aerodynamic efficiency and the aerodynamic power to be around 0.65 and 1,200W respectively. The future of polymeric materials in ORC looks promising though a long-term test using the refrigerant as the working fluid is still needed to verify material-fluid compatibility, lifespan and resistance to fatigue.

KEYWORDS

Organic Rankine Cycle; micro-turbine performance; waste heat recovery; CHP; polymer materials

1. INTRODUCTION

Waste heat recovery is a major line of action for improving the efficiency of energy systems where combined heat and power (CHP) or cogeneration can play an important role as it allows the demand of electrical and thermal energy to be satisfied in a very efficient way. Furthermore, distributed cogeneration downsized to a few-kilowatts helps for an agile response to the demand of such energy whilst reducing transmission and distribution losses. The need for distributed cogeneration in households becomes relevant when considering that the residential sector is a major contributor to the world energy consumption [1] and a significant fraction of the energy used in the sector is wasted. The cogeneration systems required by the residential sector are those of micro-capacity (under 3,000W) [2] but they are still under development with only a few products available in the market. Among the few technological options suitable for domestic cogeneration, organic Rankine cycle (ORC) has the advantages of being a mature, simple, scalable, and versatile technology. This last feature makes it possible to utilise waste heat or renewable energy as prime sources.

Micro-ORC has, however, the main shortcoming of high capital cost as exposed by Balcombe et.al. [3] and Nguyen et.al. [4], and therefore, acceptance of the technology has been limited to date. The expander is a major contributor to the problem of high capital cost, which can represent from 37% [4] to 65% [5] of the overall system cost. Moreover, the expander is also a critical component that impacts upon the reliability, operation and safety of the entire system [6]. Consequently, several investigations have been recently driven by the improvement of the expander as reported by Alshammari et.al. [7].

Although there is a wide variety of expanders, they can be classified into two categories [8, 9]: volumetric expanders (pistons, scrolls, screws and vanes) and turbo-expanders (turbines). In systems of micro-capacity, volumetric expanders are usually preferred [8-10] despite the short lifespan of wear parts and noisy operation, whereas micro-turbines are barely considered due to the perception on their cost and complexity. The fact that micro-turbines are a mature and reliable technology has been overlooked. Micro-turbines have been adopted for various applications including automotive, aerospace, energy, dental and home appliances [11-15], where simplification strategies are successfully implemented to make turbines suitable for the intended purposes. Therefore, we consider that micro-turbines are not receiving enough attention as an option for the expander in downsized ORCs, which they deserve.

A review of the literature on the limited experimental work with micro-turbines used in ORC systems with a capacity of 3,500 W or lower has revealed that micro-turbines have proven to be an efficient and reliable option for ORC expanders despite their high speed which is their most criticised characteristic. Shao et.al. [16], for example, developed a mini ORC, containing a radial micro-turbine rated at 53,500rpm rotational speed and 3,400W power output, and achieved an isentropic efficiency of 0.83 and 0.75 in their investigation [17]. Li et.al. [18] studied an ORC employing a high speed turboexpander and achieved a power output of about 700W with an isentropic efficiency of around 0.35. Pu et.al [19] tested an ORC containing a high-speed axial micro-turbine with a rated rotational speed of 18,000rpm and power of 2,000W, and achieved an isentropic efficiency of 0.59. Pei et.al. [20] studied a radial turbine rated at 60,000rpm rotational speed and 3,300W power, and achieved an isentropic efficiency of 0.65. Yagoub et.al. [21] tested a micro-turbo-generator rated at 1,500W power and 60,000rpm rotational speed, and achieved an isentropic efficiency of 0.85. Yamamoto et.al. [22] studied an inflow radial micro-turbine, rated at 45,000rpm rotational speed and 150W power, and achieved an isentropic efficiency of around 0.5. Although the successful experimentation and the achieved efficiency in these previous investigations suggest that micro-turbines can be a good option for micro-ORC expanders, the problem of high capital cost remains to be addressed.

The low temperature characteristics of ORC systems indicate the use of polymers in ORC systems is feasible. Therefore, a line of action for reducing the cost of micro-turbines may be the replacement of metals by polymers in structural elements, such as blades, wheels, casings and bearings. This simplification may help to reduce production cost of turbine parts, which consequently would reduce the cost of the entire ORC system. A review of the state of the art revealed that only a few authors have conducted experimental research on the adoption of polymers in ORC, though the scientific community is gaining interest in this field. Novotny et.al. [23], for example, proposed the adoption of polymeric parts in expanders, aiming to achieve a reduction of the cost. They fabricated a few models of turbine parts through additive manufacturing (metal laser sintering, stereo-lithography and fused deposition of polymers) and concluded that the metal laser sintering was needed when operation conditions of the prototype were demanding; however, for less-demanding conditions, such as low temperature and power, stereo-lithography and fused deposition of polymers could give satisfactory results for prototypes and small production. Zywica et.al. [24], on the other hand, performed a comprehensive assessment on the implementation of polymers for the construction of ORC expanders. They suggested the upper practical limits of temperature and pressure of 423K and 1,000kPa respectively, whereas their assessment of the mechanical integrity and the chemical compatibility suggested that the materials they selected were suitable for fabricating some subassemblies of turbines, which can have a tremendous impact in the fast development of this units.

Previously, we presented the design and analysis of a polymeric impeller for an ORC radial turbine [25] and, in this paper, we present the experimental advances on the implementation of structural polymers in an expander, intended for a micro-scale ORC. The manuscript reports the development of a variable frequency micro-turbine-generator and the test of its nozzle body and impeller, both fabricated with polymers. The aim of this work is to create an awareness of the huge potential that polymers represent as metal replacements in low-temperature ORC micro-turbines. Additionally, this work intends to give an insight of the expected performance of the micro-turbine-generator set by using a combined numerical-experimental approach. A brief description of the methods is presented first, which includes design, analysis and experimental procedures. Then the results of the investigation are presented and discussed, followed by further discussion on operation capabilities, technical performance, contribution to enhancing the economy of the micro-turbine-generator and a foreseen adoption of this technology. Lastly, the conclusions of this work are given.

2. METHODS

The general development method is comprised of six consecutive stages, as shown in Fig. 1; the specific method of each stage is described in a dedicated sub-section. In the first stage, the cycle definition is performed, where the operation conditions are set and the resulting thermodynamic boundary conditions are fed to the second stage – the design of the turbine. In the second stage, a micro-turbine-generator is designed and analysed to fulfil the conditions of operation. In the third stage, a prototype of the micro-turbine-generator is fabricated using additive manufacturing as well as traditional machining. In the fourth stage, a program for the performance simulation of the micro-turbine is developed to assess the unit at design and off-design conditions. Three simulations of the performance are performed considering air, ideal-R245fa and real-R245fa as working fluids. The results of these three simulations are expected to be similar in a dimensionless interpretation, and should therefore show a comparable performance using either air or refrigerant R245fa as the working fluid. In the fifth stage, the prototype of the micro-turbine-generator is tested using compressed air as the working fluid and the results are used to validate the simulation with air. In the sixth and final stage, the performance of the unit with the refrigerant as the working fluid is predicted, based on the dimensional similarity principle, with the simulation and the results of the test.

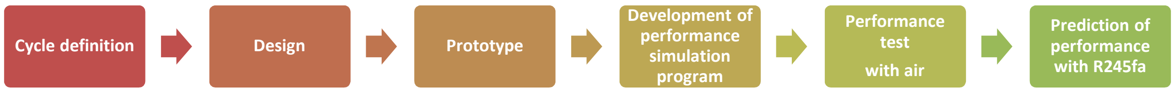

Fig. 1. Process flow diagram of the general development method.

2.1. Cycle definition

During the definition of the cycle, the heat-mass balance is made, as reported by Hernandez-Carrillo et.al. [25]; a simple ORC illustrated in Fig. 2a) with real-R245fa as the working fluid is modelled using REFPROP [26]. The heat source and sink are assumed to be streams of hot water and cold air, with evaporator and condenser temperatures of T_{evap}=328K and T_{cond}=313K respectively, though they could be changed for others with minimal thermodynamic implications. The performance of the micro-turbine-generator is estimated as aerodynamic efficiency η_{aero}= 0.7 and gross power of $\dot{W}$=1,500W. The temperature-entropy diagram of the defined ORC is shown in Fig. 2b.

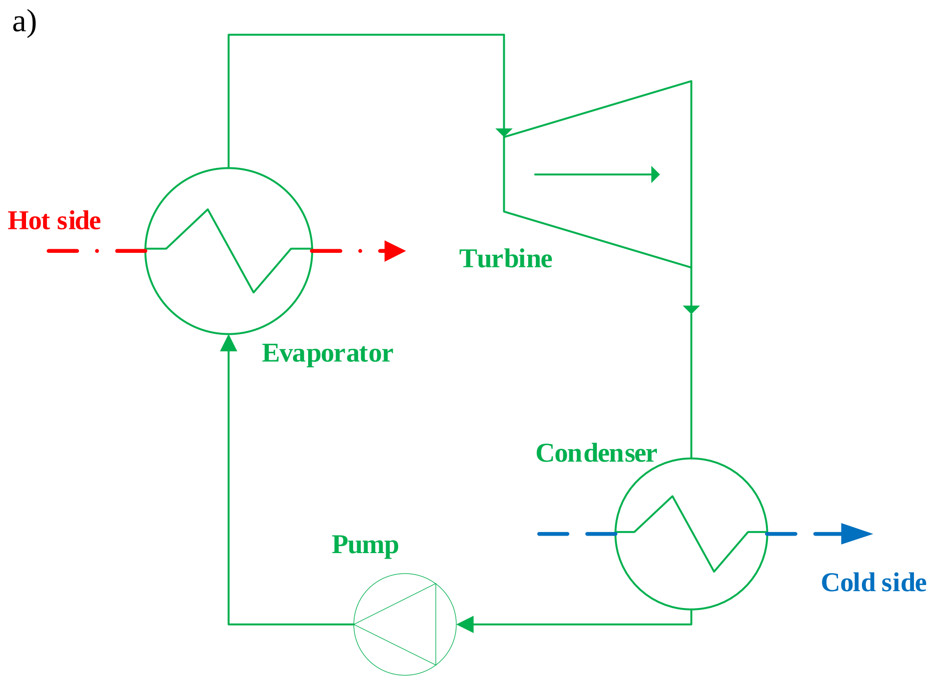

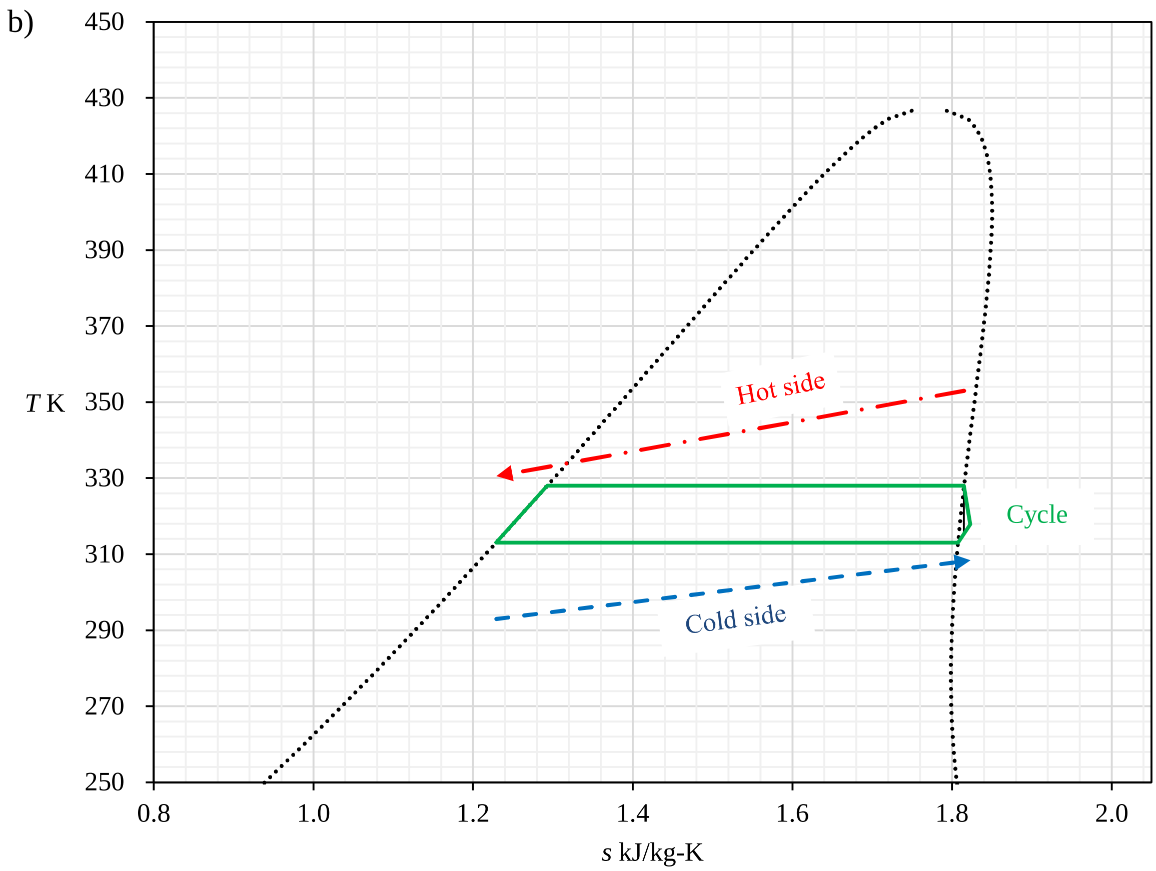

Fig. 2. Definition of the organic Rankine cycle; a) schematic of the simple configuration; b) Temperature–entropy diagram, figure adapted from [25]; *T*: Temperature, *s*: specific entropy.

2.2. Design

A radial inflow turbine is selected, *a priori*, as the expander type. The preliminary design is made through the mean-line method using the ANSYS© Vista RTD module, which uses the ideal gas law to calculate the thermo-physical properties of the working fluid. The preliminary design is then followed by a three-dimensional modelling of the nozzle body and the impeller, which are done separately using the ANSYS© BladeGen module.

The nozzle body is designed with angle-thickness definition and a uniform profile along the span of the blades. Polyethylene terephthalate glycol-modified (PETG) is selected as the structural material. The impeller, illustrated in Fig. 3a and Fig. 3b, is designed with angle-thickness definition and variable thicknesses through the span of the blades. Polyether-ether-ketone 30% glass-reinforced (PEEK-GF30) is selected as structural material based on the results of the fluid-structure-interaction (FSI) analysis performed by Hernandez-Carrillo et.al. [25]. Their study assessed the mechanical integrity of the rotor and revealed that PEEK-GF30 is 11% stronger than an aluminium in the worst condition of the application.

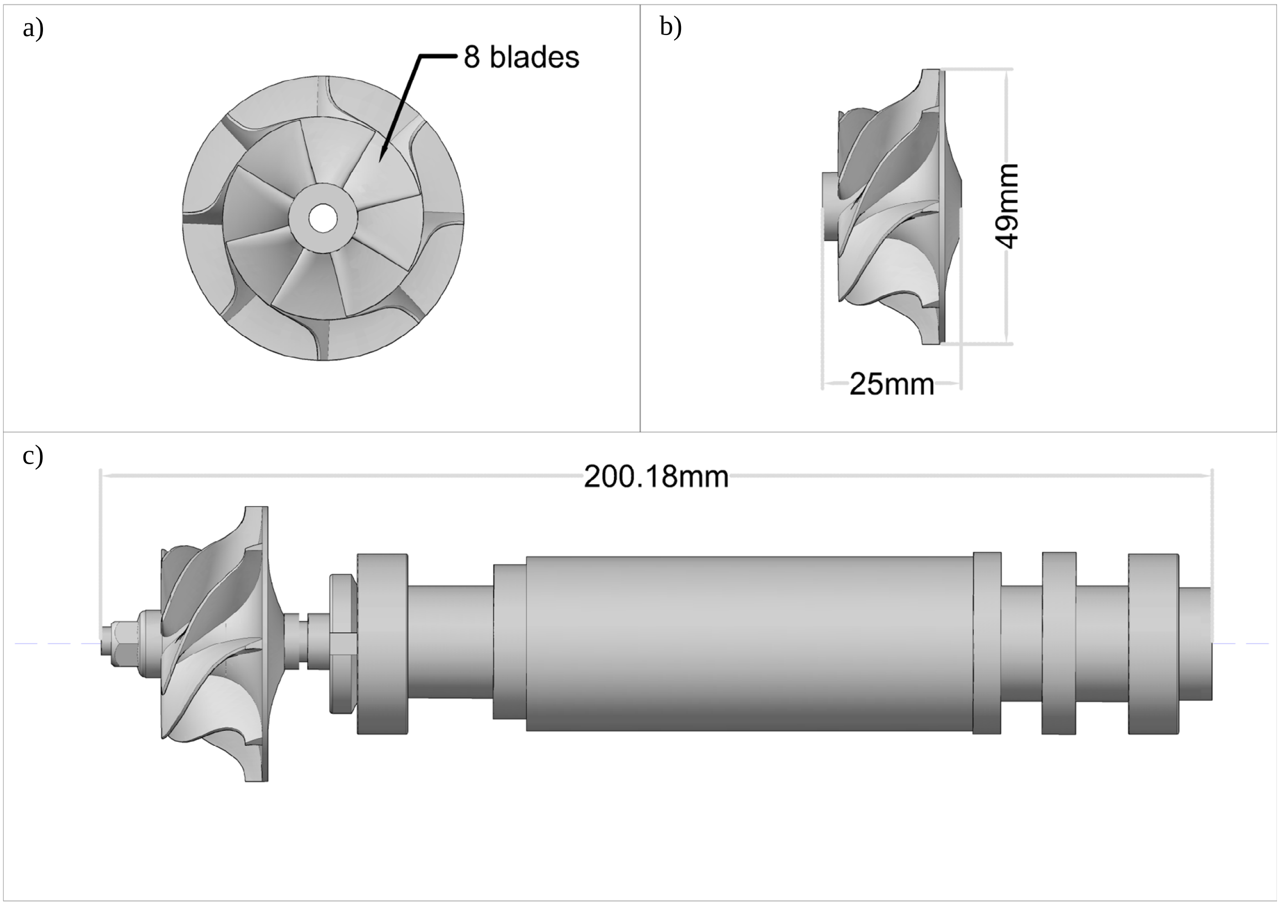

Fig. 3. Schematic of the design of the micro-turbine-generator; a) turbine impeller, front view; b) turbine impeller, lateral view; c) rotor assembly lateral view; some dimensions in the drawing might not be at real scale.

The generator, illustrated in Fig. 3c, is of the type high-speed permanent magnet directly coupled with the turbine on a common shaft. The stator is as a three-phase winding in delta connection and the rotor is a single dipole magnet.

2.3. Prototyping

The micro-turbine-generator is built using several custom-made parts and a few elements adopted from turbochargers and high-speed electric motors. The fully assembled unit is presented in Fig. 4a whose aluminium volute can be seen in the front of the micro-turbine-generator.

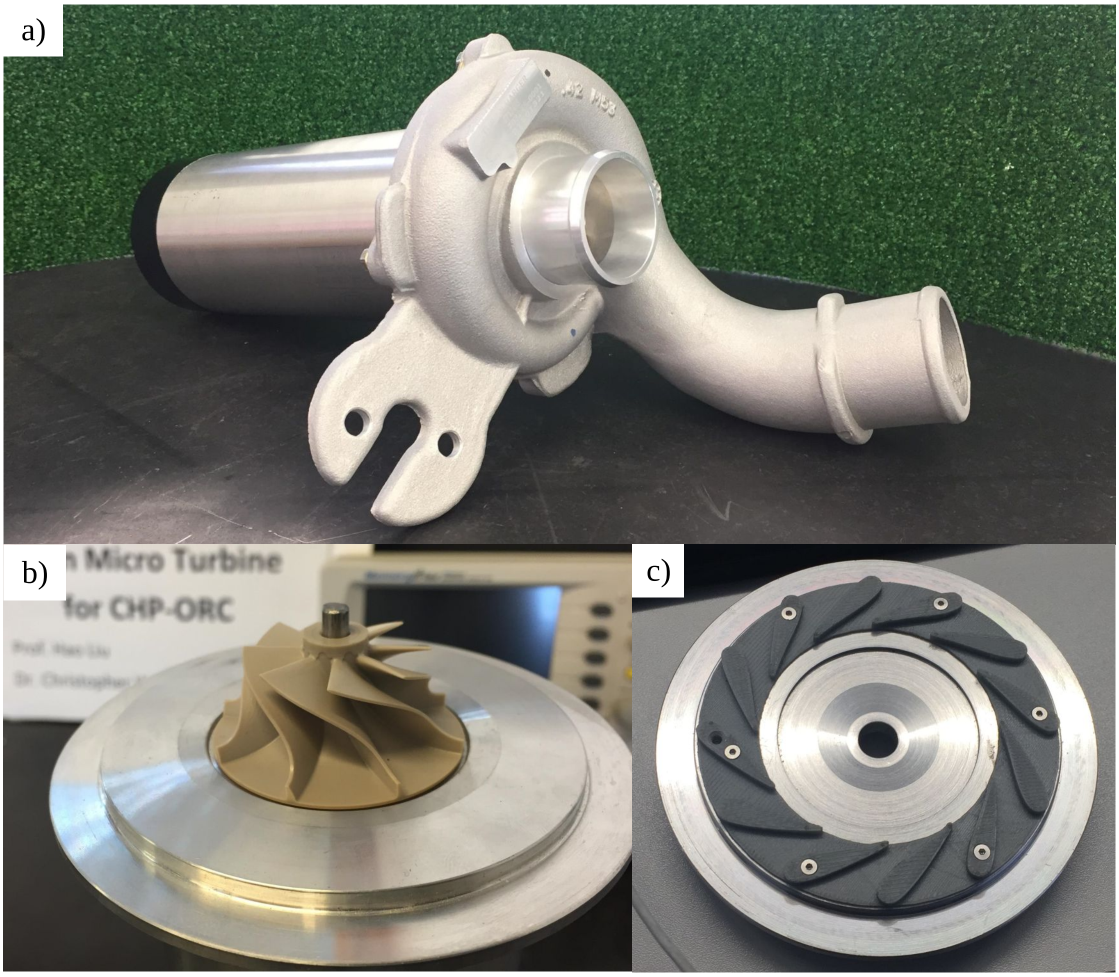

Fig. 4. Prototype of the micro-turbine-generator; a) final assembly; b) impeller of the turbine made of a polymeric material through machining; c) nozzle body of the turbine made of a polymeric material through additive manufacturing.

The nozzle body and the impeller are made of polymers; thus, they could be fabricated using mould injection. However, polymer moulding demands complex and costly equipment, which is not cost-effective for fabricating a small number of parts. Therefore, for prototyping purposes, additive manufacturing is selected to fabricate the nozzle and computational numeric machining to fabricate the impeller. The impeller, presented in Fig. 4b, is machined from a cylindric bar of PEEK-GF30 and machined into a Hurco VM10Ui five axis milling machine. The nozzle body is fabricated through polymer fused deposition with a resolution of 6.0×10^{-5} m and 100% infill density and then fastened to the baseplate of the casing, as shown in Fig. 4c. The generator, located in the rear section of the unit in Fig. 4a, consists of a stator adopted from a high speed three phase motor and a custom-made permanent magnet rotor.

2.4. Program for simulation of the performance

The assessment of the performance is done through the analysis of two parameters: the aerodynamic efficiency η_{aero} and the aerodynamic power $\dot{W}_{aero}$. A program for the simulation of the aerodynamic performance of the micro-turbine-generator is developed. The program follows the mean-line method, which assumes a single streamline flowing through the gas path with constant transversal properties, as described by Rahbar et.al [27].

The program is an iterative routine made in Microsoft Excel and Visual Basic Applications whose simplified flow-chart is presented in Fig. 5.

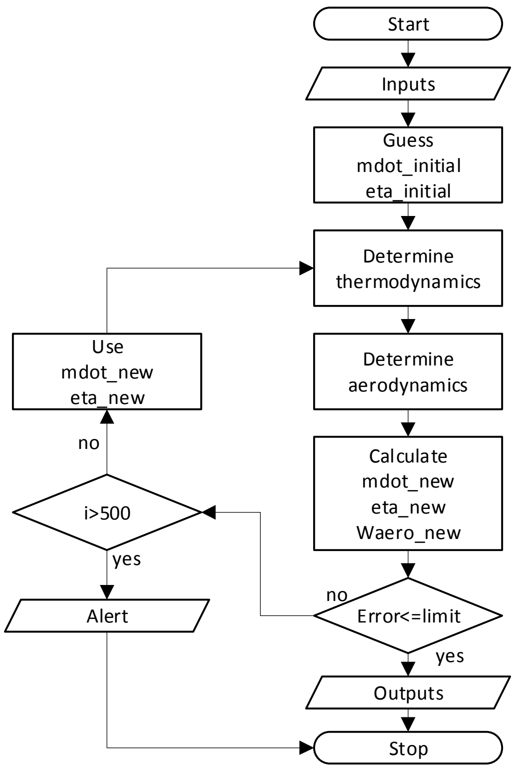

Fig. 5. Simplified flow-chart of the program for performance prediction; mdot_initial: initial guess of flowrate; eta_initial: initial guess of aerodynamic efficiency; mdot_new, calculated mass flowrate; eta_new: calculated aerodynamic efficiency; Waero_new: calculated aerodynamic power; i: iteration.

The routine successively approximates the aerodynamic efficiency, mass flow and power of the turbine. It starts reading the inputs presented in Table 1 and gives an initial guess of the aerodynamic efficiency (eta_initial) and mass flow (mdot_initial). Then, the thermo-aerodynamic equations are resolved in accordance with sections 2.4.1 and 2.4.2 and new aerodynamic efficiency (eta_new), mass flow (mdot_new) and aerodynamic power (Waero_new) are obtained and used for resolving a new iteration. The iterative cycle continues until the maximum allowed error or the maximum number of iterations are achieved; finally, the results are exported.

Table 1 Summary of inputs for the performance prediction program

Description	Symbol

Nozzle	
Inlet total temperature	T_{01}
Inlet total pressure	P_{01}
Absolute exit angle	α_2
Rotor	
Exit total pressure	P_{03}
Inlet diameter	D_2
inlet blade height / Inlet diameter	$\frac{b_2}{D_2}$
Outlet mean diameter / Inlet diameter	$\frac{D_3}{D_2}$
Exit blade height / Inlet diameter	$\frac{b_3}{D_2}$
Relative inlet angle	β_2
Relative outlet angle	β_3
Blade speed ratio	*BSR*

2.4.1. Thermodynamics

The total specific enthalpy and the total pressure across the nozzle are assumed to be constant and, therefore, the change in the static properties are given by Eqn. (1) and Eqn. (2) respectively. The actual change of the total specific enthalpy across the rotor, Δh_0, which is a function of the isentropic change of the total specific enthalpy, $\Delta h_{0s,}$ and the aerodynamic efficiency, η_{aero}, is given by the Eqn. (3).

$$h_{01} = h_{02} = h_1 + \frac{1}{2} c_1^2 = h_2 + \frac{1}{2} c_2^2 \quad (1)$$

$$P_{01} = P_{02} = P_1 + \frac{1}{2} \rho_1 c_1^2 = P_2 + \frac{1}{2} \rho_2 c_2^2 \quad (2)$$

$$h_{02} - h_{03} = \Delta h_0 = \Delta h_{0s} \eta_{aero} \quad (3)$$

The program gives the option of selecting the ideal gas law or the real gas formulation from REFPROP [26] to calculate the thermophysical properties of the fluid. When the ideal gas law is selected, the specific enthalpy and density for any given state i are calculated using Eqn. (4) and Eqn. (5) respectively; the isentropic change of specific enthalpy across the rotor is calculated with Eqn. (6).

$$h_i = c_p T_i \quad (4)$$

$$\rho_i = \frac{P_i}{R T_i} \quad (5)$$

$$\Delta h_{0s} = h_{02} - h_{03} = c_p T_{02}\left(1 - \left(\frac{P_{03}}{P_{02}}\right)^{\frac{k-1}{k}}\right) \quad (6)$$

When the real gas formulation is selected, the specific enthalpy and density for any given state i are calculated using Eqn. (7) and Eqn.(8), respectively. The isentropic change of the specific enthalpy across the rotor is calculated with Eqn. (9).

$$h_i = f_{REFPROP}(T_i, P_i) \quad (7)$$

$$\rho_i = f_{REFPROP}(T_i, P_i) \quad (8)$$

$$\Delta h_{0s} = (h_{02} - h_{03s})_{@constant\ entropy} \quad (9)$$

According with Lujan et.al. [28], the ideal gas law predicts with a reasonable accuracy the thermophysical properties of real gases at temperatures and pressures considerably lower than those at the critical point. As the range of pressure and temperature defined in section 2.1 fulfil that condition, the ideal gas formulation should calculate the properties with a maximum error of 10% with respect to the real gas formulation. Thus, the results of the simulation, at the design point, should be comparable with the results of the design tool, which relies on the ideal gas law.

2.4.2. Aerodynamics

The velocity triangles illustrated in Fig. 6 are determined by the combination of the equation of continuity, the thermodynamic equations, the nozzle geometry and the rotor geometry presented in Table 1. These triangles show the relationship of the absolute velocity c, the relative velocity w and the blade velocity u at the rotor-inlet and the rotor-outlet. The rotor-inlet is denoted with the subscript 2 and the rotor-outlet is denoted with a subscript 3; the components on the flow direction are denoted with the subscript f whereas the components on the tangential direction (movement of the blade) are denoted with the subscript u. Based on the velocity triangles, the actual change of the total specific enthalpy can be calculated using the Euler's equation for pumps and turbines, Eqn. (10).

$$\Delta h_0 = \frac{1}{2}[(c_2^2 - c_3^2) - (w_2^2 - w_3^2) + (u_2^2 - u_3^2)] \tag{10}$$

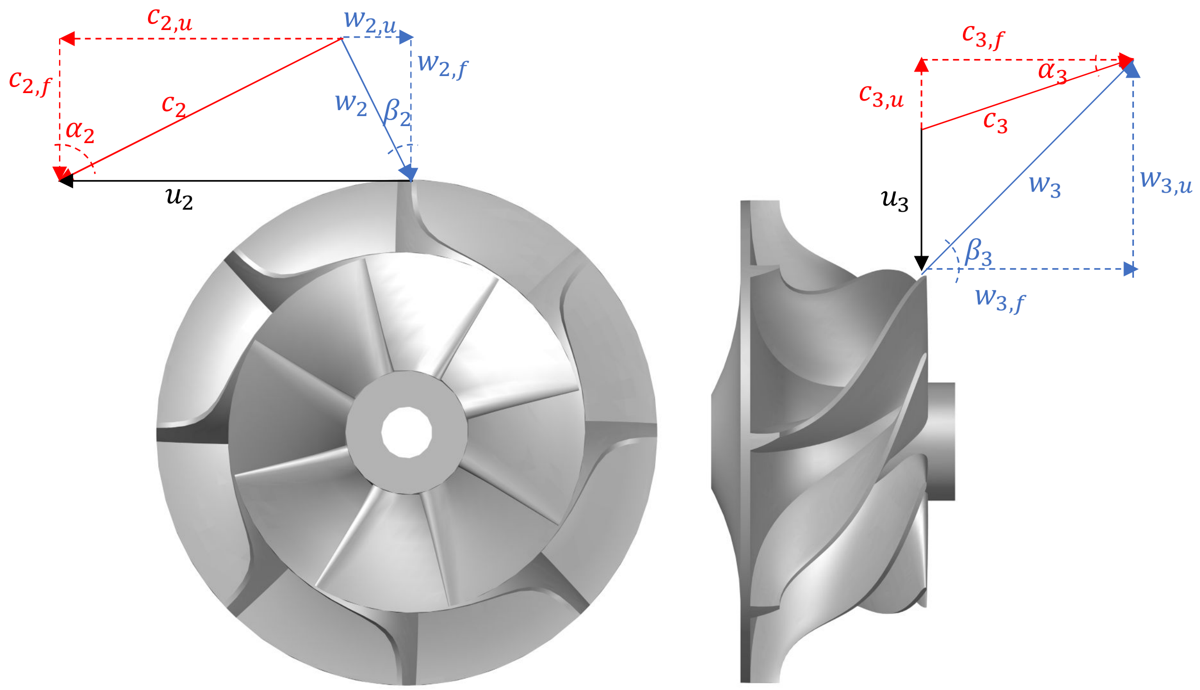

Fig. 6. Definition of the velocity triangles for the turbine rotor at off-design conditions; *c*: absolute flow speed, *u*: blade speed; *w*: relative flow speed; α: absolute angle of the flow with respect to the flow direction; β: relative angle of the flow with respect to the movement direction; 2: impeller inlet conditions; 3: impeller outlet conditions; sub index *u*: in tangential direction; sub index *f*: in the flow direction.

2.4.3. Efficiency and power

The actual aerodynamic power, $\dot{W}_{aero}$ is predicted with Eqn. (11), which is a function of the mass flowrate of working fluid, $\dot{m}$, the isentropic change of total specific enthalpy across the unit, Δh_{0s} and the aerodynamic efficiency, η_{aero}. The aerodynamic efficiency, η_{aero} is calculated with Eqn. (12), which is a function of the isentropic change of total specific enthalpy across the unit, Δh_{0s} and the aerodynamic losses, represented as an overall loss of specific enthalpy, Δh_{loss}.

Although the most employed models in literature for predicting aerodynamic losses in radial turbines are the model of Rohlik [29] and the model of Whitfield and Baines [30], the aerodynamic losses are evaluated using Eqn. (13), which follows the model proposed by Suhrmann et.al [31]. This is a compilation of models conceived for the application on low-capacity turbines; it accounts for the loss of specific enthalpy produced by: skin friction, Δh_f, secondary flow, Δh_s, incidence, Δh_i, clearance leaking, Δh_c and exiting speed, Δh_e, as illustrated in Eqn. (13).

$$\dot{W}_{aero} = \dot{m}\Delta h_0 = \dot{m}\Delta h_{0s}\eta_{aero} \quad (11)$$

$$\eta_{aero} = \frac{\Delta h_{0s} - \Delta h_{loss}}{\Delta h_{0s}} \quad (12)$$

$$\Delta h_{loss} = \Delta h_f + \Delta h_s + \Delta h_i + \Delta h_c + \Delta h_e \quad (13)$$

The skin friction loss, Δh_f is calculated with Eqn. (14), which is a function of the further corrected friction factor, $c'_{f,c}$. The further corrected friction factor is obtained from the correlation of Musgrave [32] presented in Eqn. (15), which depends on the corrected friction factor, $c_{f,c}$. The corrected friction factor is calculated with Eqn. (16), which depends on the friction factor, c_f. Lastly, the friction factor is calculated with the correlation of Colebrook et.al. [33], presented in Eqn. (17). In the aforementioned equations, the hydraulic diameter, D_h is the average ratio of the "wet" area of the gas path over its diameter, the hydraulic length, L_h is the length of the main-line of the flow, the curvature radio, r_c is the average curvature radio of the mean-line, the diameter, D_2 is defined at the rotor inlet and the average relative flow-speed across the rotor, $\overline{w}_{2-3}$ is calculated with Eqn. (18).

The secondary flow loss, Δh_s is calculated with Eqn. (19), which is a function of the rotor diameter at the inlet D_2, the number of rotor blades, Z, the curvature radio of the blades, r_c, and the flow-speed at the rotor inlet, c_2. The clearance loss, Δh_c, is calculated with Eqn. (20), which is a function of the tip clearance of the blades, tc, the height of the rotor blade at the inlet b_2 and the absolute tangential speed of the flow at the rotor inlet $c_{2,u}$. These equations for calculating secondary and leaking losses are adopted from the work of Rodgers and Geiser [34]. The incidence loss, Δh_i is calculated with Eqn. (21) proposed by Whitfield and Wallace [35], which depends on the relative tangential speed of the flow at the rotor inlet $w_{2,u}$. Finally, the exit loss, Δh_e, produced by the exiting speed, c_3, is calculated with Eqn. (22). A schematic of the cross-sectional view of a radial turbine and the geometric nomenclature used for the model is presented in Fig. 7.

$$\Delta h_f = c'_{f,c}\frac{L_h}{D_h}(\overline{w}_{2-3})^2 \quad (14)$$

$$c'_{f,c} = c_{f,c}\left[\mathrm{Re}\left(\frac{D_2}{2r_c}\right)^2\right]^{0.05} \quad (15)$$

$$c_{f,c} = c_f \left(1 + 0.075 \mathrm{Re}^{\frac{1}{4}} \sqrt{\frac{D_h}{2r_c}} \right) \tag{16}$$

$$\frac{1}{\sqrt{4c_f}} = -2 \log \left(\frac{\frac{k}{D_h}}{3.7} + \frac{2.51}{\mathrm{Re}\sqrt{4c_f}} \right) \tag{17}$$

$$\overline{w}_{2-3} = \frac{w_2 + w_3}{2} \tag{18}$$

$$\Delta h_s = \frac{D_2}{Z r_c} (c_2)^2 \tag{19}$$

$$\Delta h_c = 0.4 \frac{tc}{b_2} \left(c_{2,u}\right)^2 \tag{20}$$

$$\Delta h_i = \frac{1}{2} \left(w_{2,u}\right)^2 \tag{21}$$

$$\Delta h_e = \frac{1}{2} (c_3)^2 \tag{22}$$

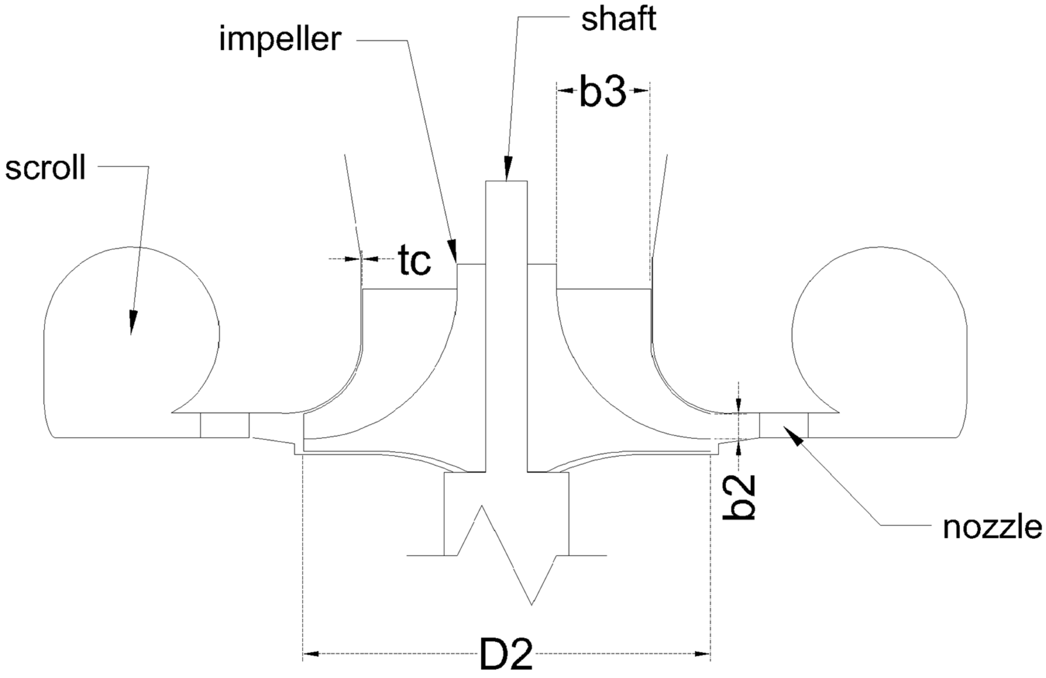

Fig. 7. Schematic of the cross-sectional view of a radial turbine and the nomenclature for the modelling; D2: rotor inlet diameter; b2: rotor inlet blade height; b3: rotor outlet blade height; tc: tip clearance.

2.4.4. Mass flow

The mass flow can be iteratively obtained by simultaneously solving all the above equations and the equation of continuity for a volume of control shown in Eqn. (23).

$$\dot{m} = \rho_2 A_2 c_{f,2} = \rho_3 A_3 c_{f,3} \tag{23}$$

2.4.5. Dimensionless interpretation

The most important parameter for assessing the performance of the micro-turbine-generator is the aerodynamic efficiency. It can be represented as a function of two dimensionless parameters: the flow coefficient ϕ and the loading coefficient, ψ, defined in Eqns. (24) and Eqn. (25), respectively. The aerodynamic efficiency is, thus, three-dimensional in a space $\phi - \psi - \eta_{aero}$, which is commonly presented in Smith [**36**] type charts. These charts show contours of aerodynamic efficiency in a plane $\phi - \psi$ or, in other words, the projection of the three-dimensional efficiency in such a plane. However, for convenience, the results in this work are presented in four separate charts that are projections of the three-dimensional efficiency in different planes.

$$\phi = \frac{c_{f,2}}{u_2} \tag{24}$$

$$\psi = \frac{\Delta h_{0S}}{u_2^2} \tag{25}$$

The first chart is a representation of the relationship of the flow coefficient ϕ and the loading coefficient ψ but the linearized parameter $\sqrt{2\psi}$ is used instead of ψ; this means that such a chart is the representation of the efficiency in the plane $\phi - \sqrt{2\psi}$. This chart is homologous to the maps of radial turbines, adopted by Alshammari et.al. [37] for example, to describe the relationship between the corrected mass flow rate $\dot{m}_c$ and the expansion ratio PR. Comparably, the flow coefficient and the corrected mass flow rate represent the mass flow rate whereas the loading coefficient and the expansion ratio represent the expansion. The representation with the flow and loading coefficients is, however, more convenient when presented in a $\phi - \sqrt{2\psi}$ plane, where such a relationship describes a straight line. The second chart is a projection of the efficiency in a plane $\phi - \eta_{aero}$ and the third chart is a projection of the efficiency in a plane $\sqrt{2\psi} - \eta_{aero}$. Finally, the fourth chart is a handy representation of the efficiency that shows the efficiency in a plane $BSR - \boldsymbol{\eta_{aero}}$, with BSR being the blade speed ratio presented in Eqn. (26). This chart is analogous to the representation in a plane of $\sqrt{2\psi} - \eta_{aero}$ because the blade speed ratio BSR is a function of the loading coefficient ψ. However, the chart $BSR - \eta_{aero}$ is more common in specialised literature for representing the performance of radial inflow turbines as Dixon and Hall [38] had demonstrated.

$$BSR = \frac{u_2}{C_0} = \frac{1}{\sqrt{2\psi}} \tag{26}$$

2.5. Experimental validation through a performance test with air

The simulation program is validated through a performance test under similar conditions; this means that the test is performed using air as the working fluid instead of the refrigerant and dynamic similarity of the flow is assured. With this technique, the aerodynamic performance of the unit should be confidently extrapolated through the principle of dynamic similarity to the real operational conditions, i.e. the unit working with refrigerant as the working fluid.

2.5.1. Procedure

The test rig is comprised of the micro-turbine-generator, a safety envelope, a supply system of compressed air, an electric load bank and monitoring instrumentation. The safety envelope is a 304 stainless steel tank with internal baffles for burst containment. The air supply system consists of a GX7FF compressor, a pneumatic regulator, a main control valve, a shutoff valve, piping and hose connections. The load bank is a three-phase array of electric bulbs with fused switches. The schematic of the performance testing rig is shown in Fig. 8a and the photo of the test rig with the key equipment clearly marked is shown in Fig. 8b, whereas the instrumentation of the test rig is described in section 2.5.3.

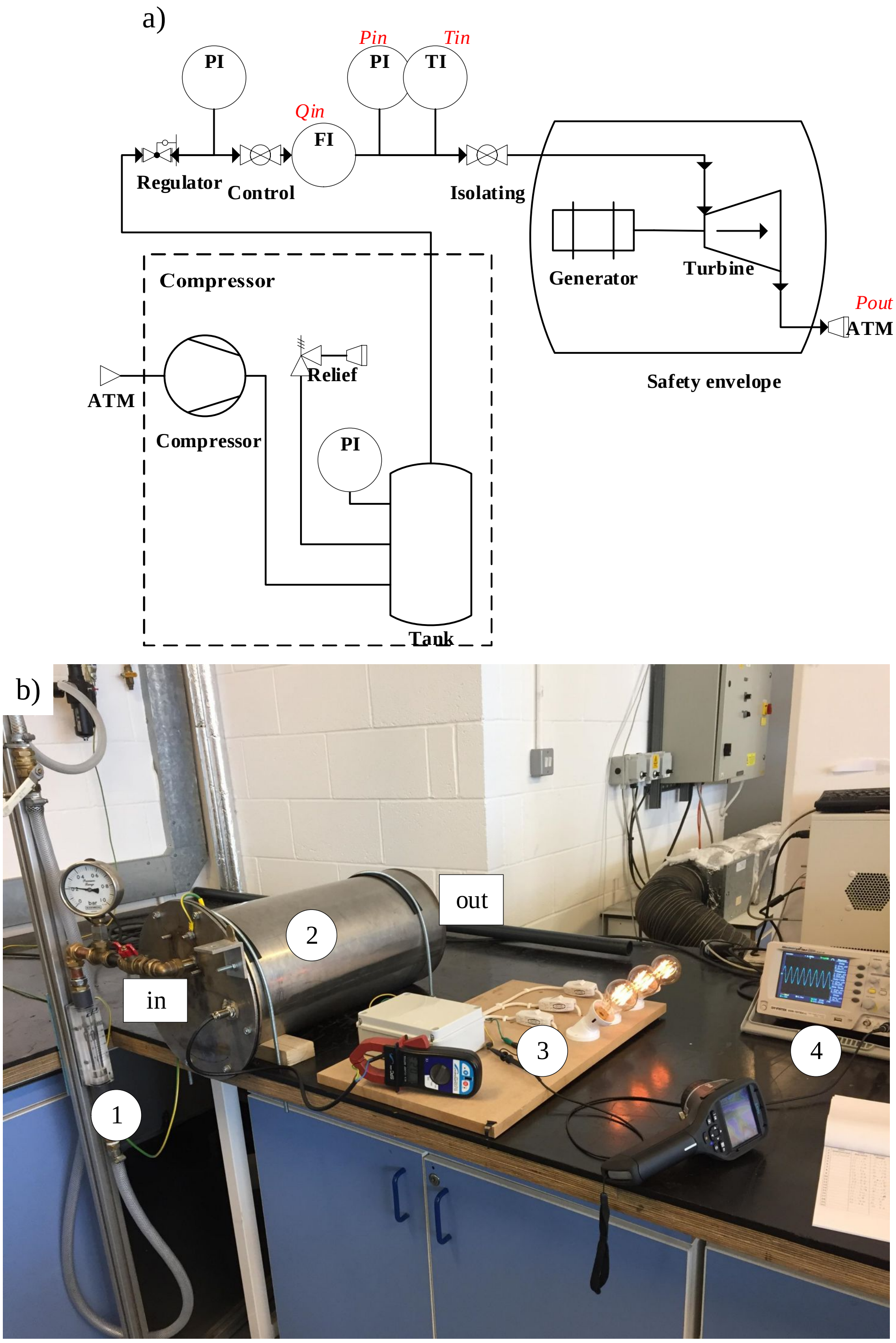

Fig. 8. Test rig using compressed air: a) schematic set up; b) photo of the actual array; Q_{in}: volume flow rate at inlet; P_{in}: static pressure at inlet; T_{in}: static temperature at inlet; P_{out}: static pressure at outlet; PI: pressure indicator, TI: temperature indicator, FI: flowrate indicator; ATM: atmosphere; 1: air supply, 2: safety envelope, 3: load bank, 4: monitoring oscilloscope.

A stream of compressed air is supplied to the rig at the point labelled as “in” and discharged to the atmosphere at the point labelled as “out” at the back of the rig (both “in” and “out” are indicated in Fig. 8b). Conventionally, the performance test of turbines is performed at nominal capacity (or fractions of it) and the nominal rotational speed (or selected fractions of it). Additionally, the rotational speed is controlled with a governor that responds to variations of the load keeping the speed constant. In this study, however, the unit comprises a variable frequency turbine not equipped with a governor, because the control of the unit lies on a controlled expansion ratio. Consequently, the rotational speed responds to changes of the load and conventional testing methods may not suit the requirements of this application. Thus, a simple procedure for the test consisting of ten simple steps, described below, is defined.

I. Perform preliminary checks, ensure the control valve is fully closed and the isolation valve is fully open, supply compressed air to the system.
II. Connect the first load combination.
III. Initiate the trial by opening the control valve until achieving a rotational speed ω=3,000rpm.
IV. Let the unit settle down, 15 minutes for the first trial and 5 minutes for subsequent trials, to allow bearings and lubricants to warm up.
V. Let the unit settle down 10 minutes for the parameters to achieve a steady state.
VI. Register the parameters in the corresponding sheet and number the register as a record.
VII. If the control valve is fully open, proceed to step VIII, otherwise, open the control valve to increase the inlet pressure ΔP_{in}=2kPa and repeat from step V for starting a new record.
VIII. If three trials have been recorded for the current load, proceed to step IX, otherwise, close the control valve to reset the rotational speed to ω=3,000rpm and repeat from step IV for starting a new trial.
IX. If the total number of loads have been tested, proceed to step X, otherwise, connect the next load and repeat from step III.
X. Fully close the control valve, fully close the isolation valve and suspend the supply of compressed air.

The test is performed with a close monitoring of the unit while a register of measurements from the instruments is maintained. A set of readings of the experimental parameters for a given time is called a record, whereas a set of 8 records at 0.25, 0.37, 0.50, 0.6, 0.7, 0.8, 0.9 and 1 of span of the inlet pressure is called a trial. Three different loads are tested: load 1 consists of three 40W bulb connected to the phases a, b and c, load 2 consists of two 40W bulb connected to the phases a and b, respectively, and load 3 consists of one 40W bulb connected to the phase a. Thus, a total of 72 records are generated in the test, as shown in in Table 2. The records

1 to 24 correspond to the trials 1, 2 and 3 of load 1; the records 25 to 48 correspond to the trails 4, 5 and 6 of load 2; the records 49 to 72 correspond to the trials 7, 8 and 9 of load 3. This assured repeatability of the test.

Table 2 Convention for numbering records, trials and loads for the experimental test.

		Record number							
	Span of P_{in}	0.25	0.37	0.5	0.6	0.70	0.8	0.9	1
Load1	Trial1	1	2	3	4	5	6	7	8
	Trial2	9	10	11	12	13	14	15	16
	Trial3	17	18	19	20	21	22	23	24
Load2	Trial4	25	26	27	28	29	30	31	32
	Trial5	33	34	35	36	37	38	39	40
	Trial6	41	42	43	44	45	46	47	48
Load3	Trial7	49	50	51	52	53	54	55	56
	Trial8	57	58	59	60	61	62	63	64
	Trial9	65	66	67	68	69	70	71	72

2.5.2. **Experimental determination of the dimensionless parameters**

The heat losses at the inlet and outlet are negligible and therefore, the thermo-aerodynamic analysis is also valid for the testing boundary conditions "in" and "out" as defined in the procedure. The total specific enthalpy and the total pressure can then be assumed constant across the inlet and the outlet.

In conventional applications, the mechanical and electrical losses are not a considerable fraction of the aerodynamic power and the aerodynamic efficiency is approximately equal to the electromechanical efficiency measured at the brake. For this reason, the electromechanical efficiency can be reasonably extrapolated through dynamic similarity of the flow. In this study, however, the mechanical and electrical losses account for a considerable fraction of the aerodynamic power and, consequently they must be accounted in the test and considered for the determination of the aerodynamic efficiency.

Aerodynamic efficiency

The aerodynamic efficiency η_{aero} can be experimentally obtained from Eqn. (27), which is a function of the power consumed in the load bank, $\dot{W}_{bank}$, the mechanical losses $\dot{W}_m$ and the electrical losses $\dot{W}_e$. Then, the Eqn. (12) and Eqn. (27) can be used for the comparison of analytical and experimental results.

$$\eta_{aero} = \left(\frac{\dot{W}_{bank} + \dot{W}_m + \dot{W}_e}{\dot{m} \Delta h_{0s}} \right) \tag{27}$$

The power measured at the load bank $\dot{W}_{bank}$ can be calculated with Eqn. (28), which is a function of the root mean square voltage V_{rms} and current I_{rms} in the windings. It should be pointed out that the voltage V_{rms} is the uniform in all the phases, whereas the current I_{rms} is the average value among the three phases a, b and c of the generator, in accordance with Eqn. (29).

$$\dot{W}_{bank} = \sqrt{3}V_{rms}I_{rms} \tag{28}$$

$$I_{rms} = \frac{I_{rms}^{a} + I_{rms}^{b} + I_{rms}^{c}}{3} \tag{29}$$

The mechanical loss $\dot{W}_m$ produced by friction in the bearings is obtained from Eqn. (30), which requires the frictional moment τ_m. This is a very small dynamic moment with an absolute value within the range of $\tau_m \in (2.0\text{x}10^{-2}\text{-}1.0\text{x}10^{-1})$ N-m, which is difficult to measure as it requires sophisticated equipment that is unavailable at the time of testing. Consequently, the frictional moment is estimated through the mathematical model provided by the manufacturer [39].

$$\dot{W}_m = 2(2\pi f)\tau_m \tag{30}$$

The electrical loss $\dot{W}_e$ produced by joule effect through the generator windings can be determined with Eqn. (31), which is a function of the mean root square current I_{rms} in the windings and the internal resistance R_w per phase.

$$\dot{W}_e = \sqrt{3}I_{rms}^{2}R_w \tag{31}$$

Flow and loading coefficients

With a careful examination of the thermo-aerodynamic analysis, it can be realised that the flow and loading coefficients can be experimentally determined if the seventeen parameters presented in Table 3 are known. These parameters can be classified as either ‘variable’ or ‘constant’ throughout the test. Variables are those parameters that change and must be continuously monitored, whereas constants are those parameters that are not expected to change and can be measured only once throughout the test or assumed as a constant reference value.

Table 3 Experimental parameters

#	Parameter	Symbol	Type	Source
1	Current, root mean squared phase a	I_{rms}^{a}	Variable	Measured
2	Current, root mean squared phase b	I_{rms}^{b}	Variable	Measured
3	Current, root mean squared phase c	I_{rms}^{c}	Variable	Measured

4	Frequency	f	Variable	Measured
5	Pressure, static inlet	P_{in}	Variable	Measured
6	Temperature, static inlet	T_{in}	Variable	Measured
7	Voltage, root mean squared	V_{rms}	Variable	Measured
8	Volume flow rate, inlet	Q_{in}	Variable	Measured
9	Diameter, inlet	D_{in}	Constant	Measured
10	Diameter, outlet	D_{out}	Constant	Measured
11	Diameter, rotor-inlet	D_2	Constant	Measured
12	Height, blade rotor-inlet	b_2	Constant	Measured
13	Resistance, generator windings resistance per phase	R_w	Constant	Measured
14	Angle, nozzle exit	α_2	Constant	Referenced
15	Coefficient, heat capacity at constant pressure	c_p	Constant	Referenced
16	Coefficient, isentropic expansion	k	Constant	Referenced
17	Pressure, static outlet	P_{out}	Constant	Referenced

2.5.3. Measurement devices and error propagation

The experimental parameters are defined and/or measured as explained below. The nozzle exit angle is extracted from the design stage of this work. The real gas heat capacity c_p=1,005J/kg-K and the coefficient of isentropic expansion k=1.4 are assumed to be constant and taken from the specialised literature [40]. The outlet pressure P_{out}=101.9kPa is assumed to be constant and equal to the average atmospheric pressure recorded in September 2018 at the UK East Midlands weather station [41]. The root mean squared electric current per phase I_{rms}^a, I_{rms}^b and I_{rms}^c are measured with a clamp ammeter. The frequency f and the root mean squared voltage V_{rms} are measured with a two-channel oscilloscope. The inlet static pressure P_{in} is measured with a pressure gauge. The inlet static temperature T_{in} is measured with an electronic thermometer. The inlet volume flowrate Q_{in} is measured with a variable area flowmeter (rotameter). The inlet, outlet and rotor inlet diameters D_{in}, D_{out}, D_2, and the blade height b_2 are measured with a digital caliper. The electrical resistance R_w of the generator windings is measured with an ohmmeter. Table 4 presents details of all the instruments used during the test.

Table 4 Instruments used for the measurement of the parameters

Parameter	Quantity	Units	Instrument	Range	Accuracy
I_{rms}^a	Current	A	Ammeter	0 to 2	0.01A
I_{rms}^b	Current	A	Ammeter	0 to 2	0.01A
I_{rms}^c	Current	A	Ammeter	0 to 2	0.01A
f	Frequency	Hz	Oscilloscope	10 to 7×10^6	2% of reading
P_{in}	Gauge pressure	kPa	Manometer	0 to 100	1.6kPa
T_{in}	Temperature	K	Electronic thermometer	323 to 1,573	2.5K
V_{rms}	Electric potential difference	V	Oscilloscope	0 to 600	2% reading
Q_{in}	Flow rate	m^3/s	Rotameter	0 to 2.4×10^{-2}	7.2×10^{-4} m^3/s
D_{in}	Length	m	Calliper	1 to 0.2	1×10^{-5}m
D_{out}	Length	m	Calliper	1 to 0.2	1×10^{-5}m
D_2	Length	m	Calliper	1 to 0.2	1×10^{-5}m
b_2	Length	m	Calliper	1 to 0.2	1×10^{-5}m
R_w	Resistance	Ω	Ohmmeter	0-200	0.8% of reading

The dimensionless parameters of interest are not measured but calculated with the experimental parameters, thus an analysis of propagation of errors must be performed to assess how the errors of measurements affect the dimensionless parameters. Such an analysis is made using the software Maple-2017 where the uncertainties of the experimental parameters reported in Table 4 are combined with the equations of the thermo-aerodynamic analysis. The results are shown in Table 5 and suggest that the aerodynamic efficiency can be obtained with a maximum uncertainty of 9%, the flow coefficient with maximum uncertainty of 4% and $\sqrt{2\psi}$ with a maximum uncertainty of 4%.

Table 5 Results of the analysis of propagation of error

Parameter	Value	Uncertainty	Referred to the value
η_{aero}	0.632	$5.90\text{x}10^{-2}$	9%
ϕ	0.406	$1.69\text{x}10^{-2}$	4%
$\sqrt{2\psi}$	2.163	$8.48\text{x}10^{-2}$	4%

2.6. Prediction of the performance with refrigerant

Once the simulation program is validated with the air test, the performance of the micro-turbine-generator working with the refrigerant R245fa can be predicted. The performance of turbomachines is similar if they have geometric and dynamic similarity; this principle has been extensively explained by Dixon and Hall [38] and implemented by Zhang et.al [42] and White and Sayma [43]. The geometry of the turbine does not change throughout this investigation; thus, the flow can be considered dynamically similar for identical values of the flow coefficient ϕ and $\sqrt{2\psi}$. Accordingly, the aerodynamic efficiency should be comparable in different scenarios, for example air, ideal-R245fa, or real-R245fa as working fluids, if the flow coefficient ϕ and $\sqrt{2\psi}$ are identical, as shown in Eqn. (32).

$$\eta_{aero}^{real-R245fa} \cong \eta_{aero}^{ideal-R245fa} \cong \eta_{aero}^{air} = f(\phi, \sqrt{2\psi}) \tag{32}$$

3. RESULTS AND DISCUSSION

In this section, the results of the simulation and the test are presented and discussed, with an aim of validating the simulation program via the correlation to the test results. Additionally, both, the test with compressed air and the simulations with air will be used to predict the performance of the micro-turbine-generator operating with R245fa as the working fluid.

3.1. Simulation of the performance

The program for performance simulation described in section 2.4 presented a good agreement with the design tool, at the design point, using both ideal-R245fa and air as working fluids. Additionally, the program shows a deviation under 10% for the off-design performance. This can be observed in Fig. 9, which shows the simulation with air, air with ±10% error, ideal-R245fa and real-R245fa as the working fluid. The results in the plane $\phi - \sqrt{2\psi}$ are shown in Fig. 9a where the parameter $\sqrt{2\psi}$ with respect to ϕ follows a straight line with a positive slope, which is expected for an ungoverned turbine. As shown in Fig.9a, the deviations of the simulations for ideal-R245fa and real-R245fa with respect to air increase for large values of ϕ and $\sqrt{2\psi}$, though the differences remain under 10% error. On the other hand, the results in the planes $\phi - \eta_{aero}$ and $\sqrt{2\psi} - \eta_{aero}$, shown in Fig. 9b and Fig. 9c, respectively, predict a maximum aerodynamic efficiency of η_{aero}=0.66 at the values ϕ=0.3, $\sqrt{2\psi}$=1.6, and ψ=1.3. The aerodynamic efficiency could be higher according to the White-Sayma [44] if the flow coefficient of ϕ=0.3 and a loading coefficient ψ=0.95 could be achieved. However, the simulated aerodynamic efficiency seems to be within the range reported in experimental literature [16-22].

a)

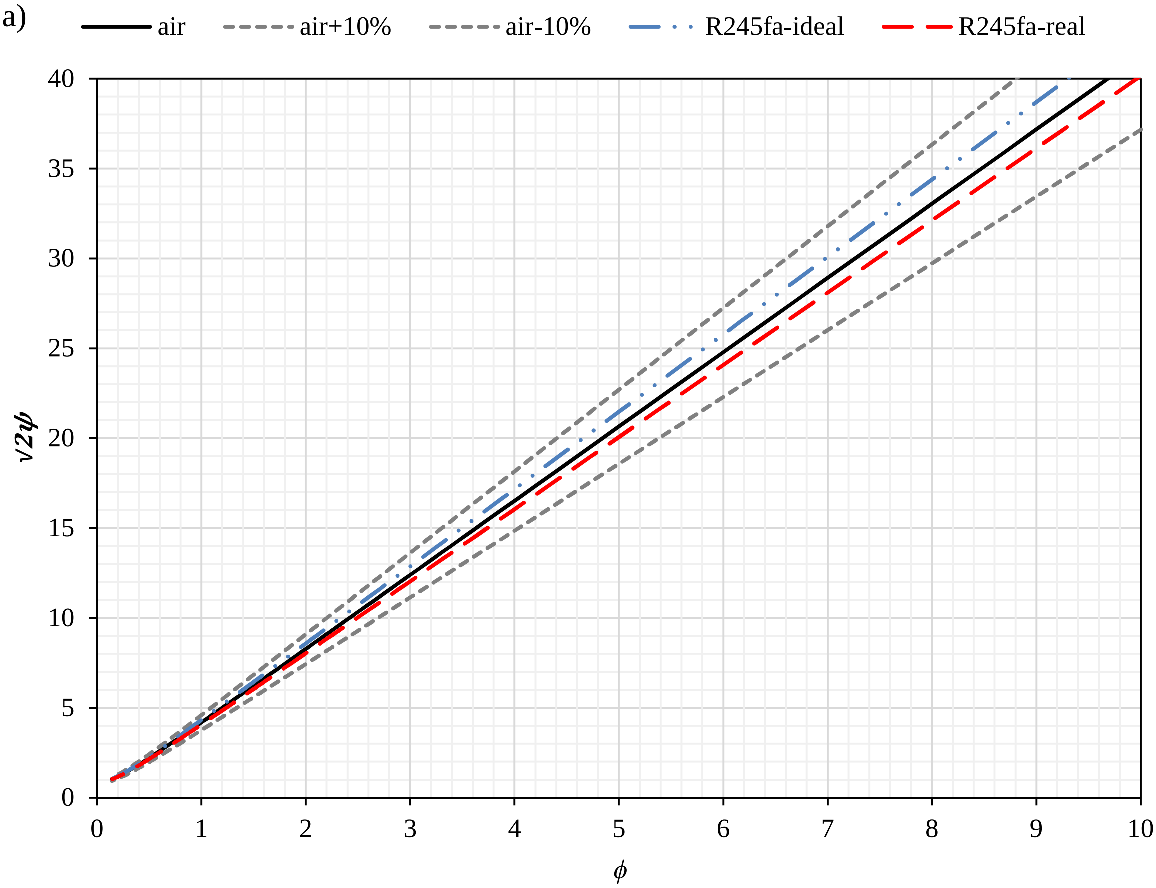

b)

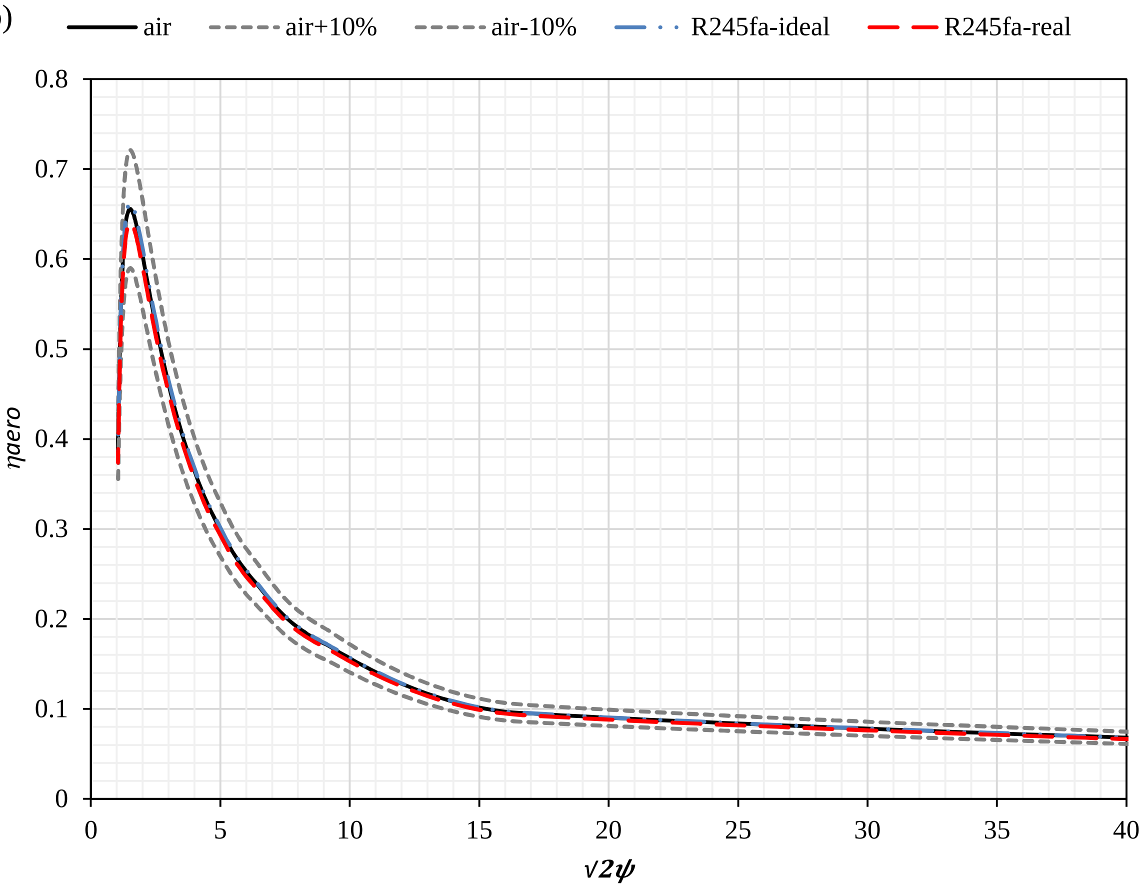
air
air+10%
air-10%
R245fa-ideal
R245fa-real
0.8
0.7
0.6
0.5
0.4
0.3
0.2
0.1
0
ηaero
0
5
10
15
20
25
30
35
40
√2ψ

406

c)

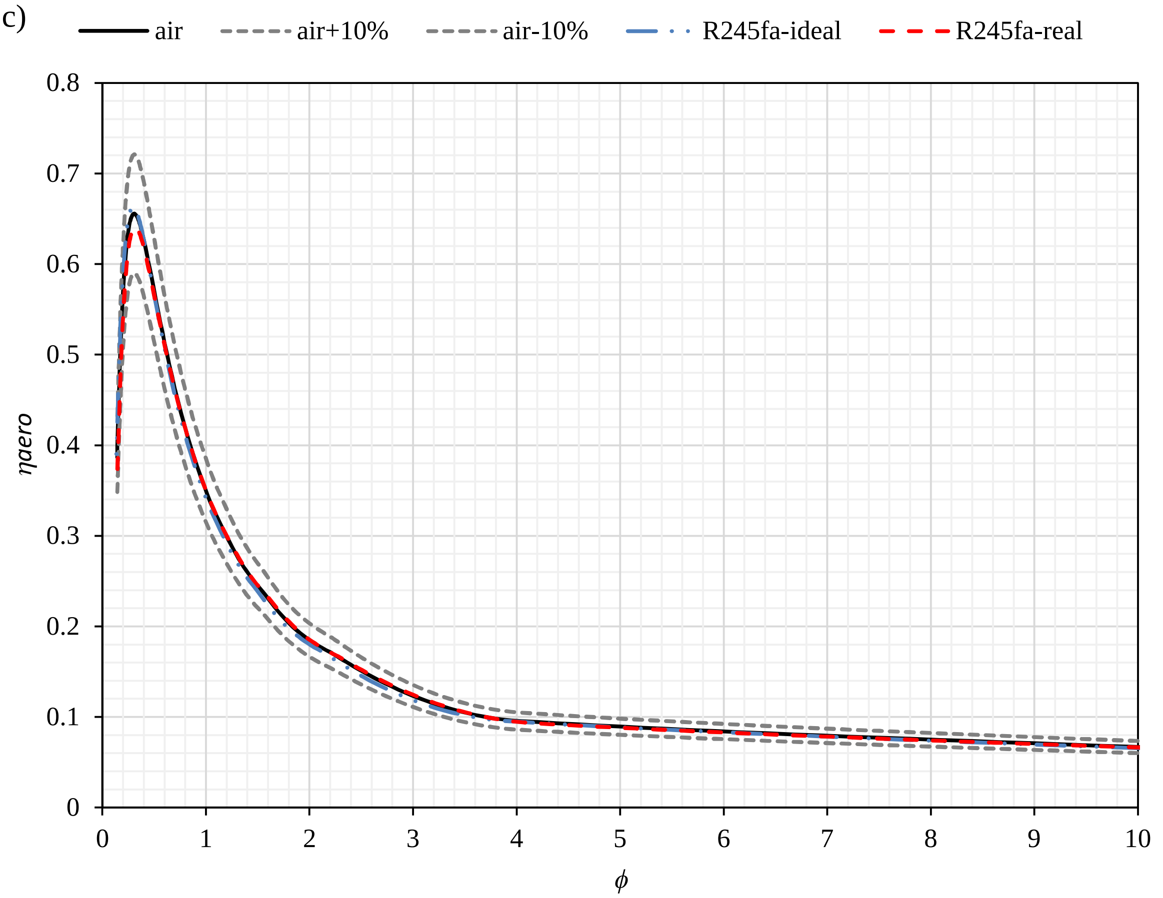
air
air+10%
air-10%
R245fa-ideal
R245fa-real
0.8
0.7
0.6
0.5
0.4
0.3
0.2
0.1
0
ηaero
0
1
2
3
4
5
6
7
8
9
10
ϕ

407

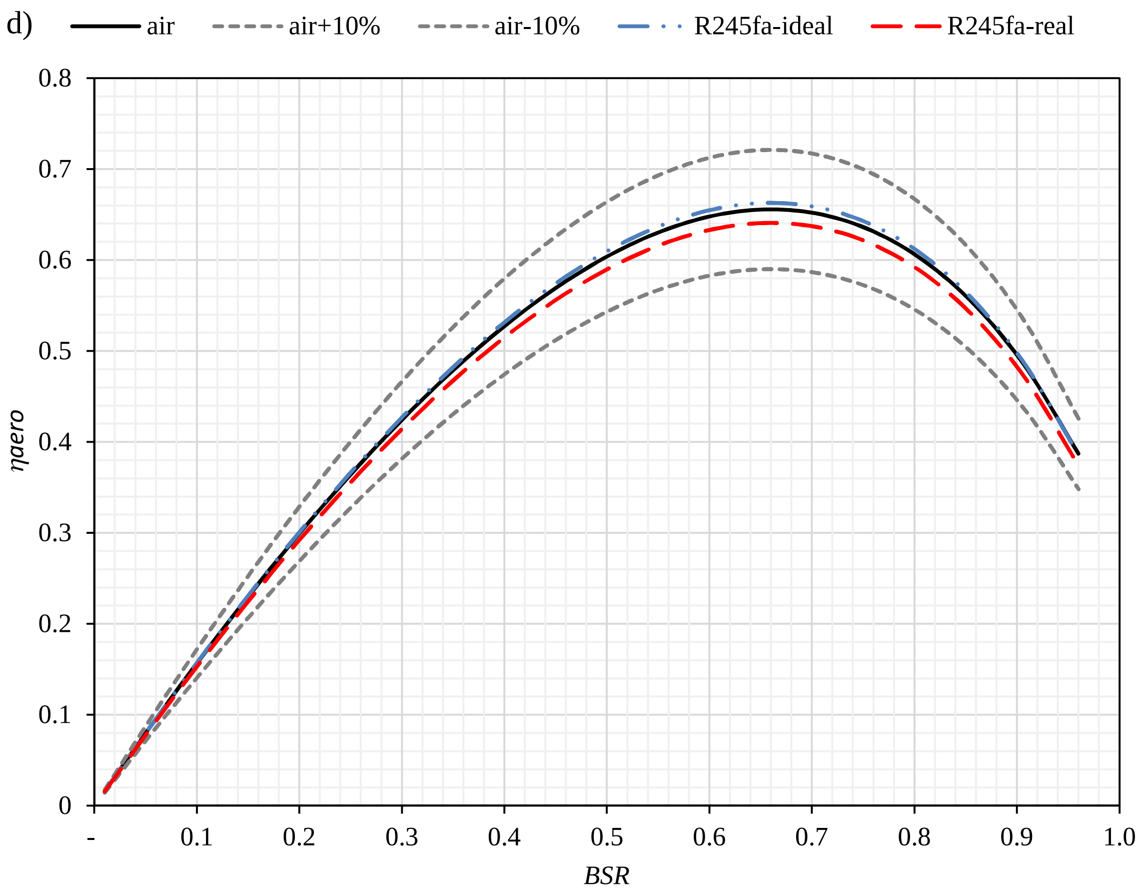

Fig. 9. Comparison of the performance between simulation with air, simulation with air ±10% error, simulation with ideal-R245fa and simulation with real R245fa; a) plane $\phi - \sqrt{2\psi}$; b) plane $\sqrt{2\psi} - \eta_{aero}$; c) plane $\phi - \eta_{aero}$; d) plane $BSR - \eta_{aero}$; ϕ: flow coefficient, ψ: loading coefficient, *BSR*: blade speed ratio, η_{aero}: aerodynamic efficiency.

The results in the plane $BSR - \eta_{aero}$ show a typical behaviour of a radial inflow turbine where the maximum aerodynamic efficiency η_{aero}=0.66 corresponds to a blade speed ratio of *BSR*=0.66 as can be seen in Fig. 9d. Additionally, a good agreement between the simulation with air, ideal-R245fa and real-R245fa is also evident. As a conclusion, it can be said that the simulation program is expected to give an acceptable insight of the performance in a dimensionless interpretation. Moreover, the error remains under ±10% in the calculation of the aerodynamic efficiency between air, ideal-R245fa and real-R245fa as the working fluid. This suggests that the dimensionless performance is equivalent for the three studied working fluids.

3.2. Performance test with air

The unit exhibited a stable behaviour during the test with compressed air while operating at off-design conditions. Although the design point could not be reached due to limitations on the air supply system, the results provided enough information to conclude about its performance. The experimental parameters are recorded and presented in a reduced form in Fig. 10. A total of 72 records are generated in the test as described in Table 2. A summarised register of the thermodynamic parameters is shown in Fig. 10a whereas a register of the electric parameters is shown in Fig. 10b. In these figures, the reduced form is a dimensionless way to represent the parameters referred to its maximum and minimum limits throughout the experiment. The calculation of the reduced frequency f^r is presented as an example in Eqn. (33), where the reduced form is denoted with the superscript r and its maximum and minimum limits are denoted with the subscripts max and min, respectively, all the parameters are reduced analogously.

$$f^r = \frac{f - f_{min}}{f_{max} - f_{min}} \tag{33}$$

a)

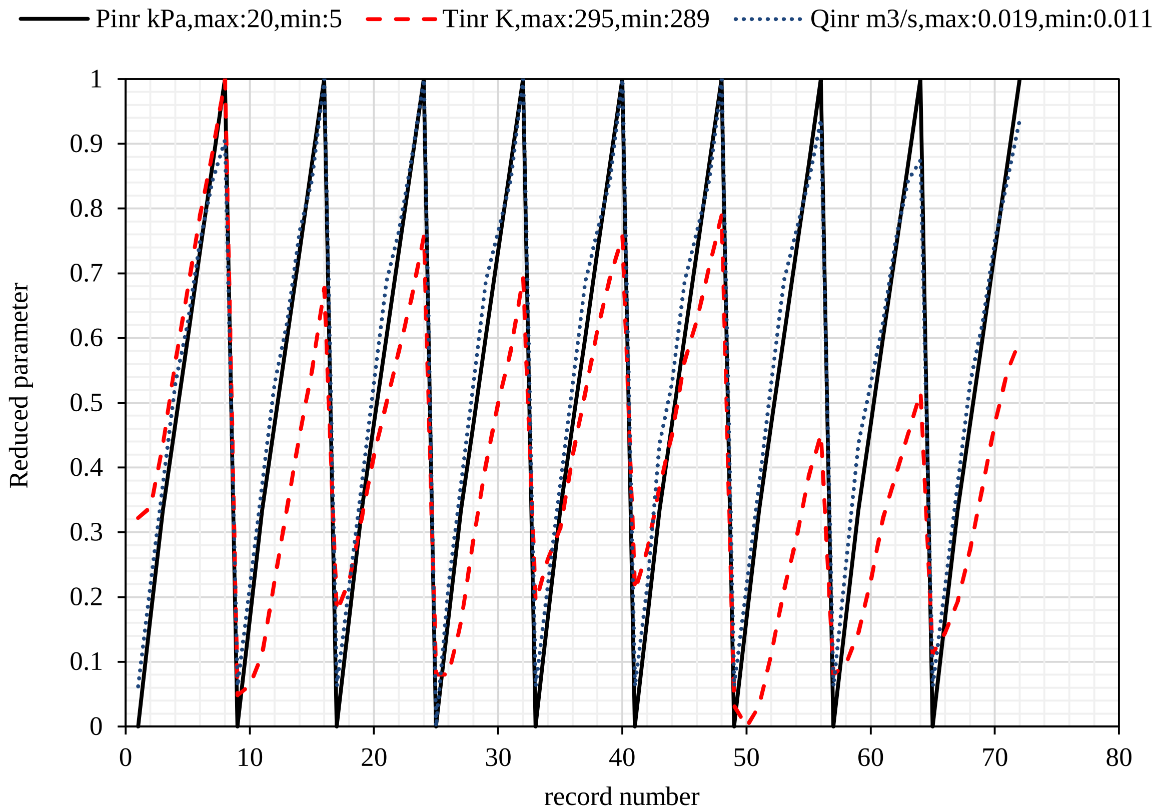

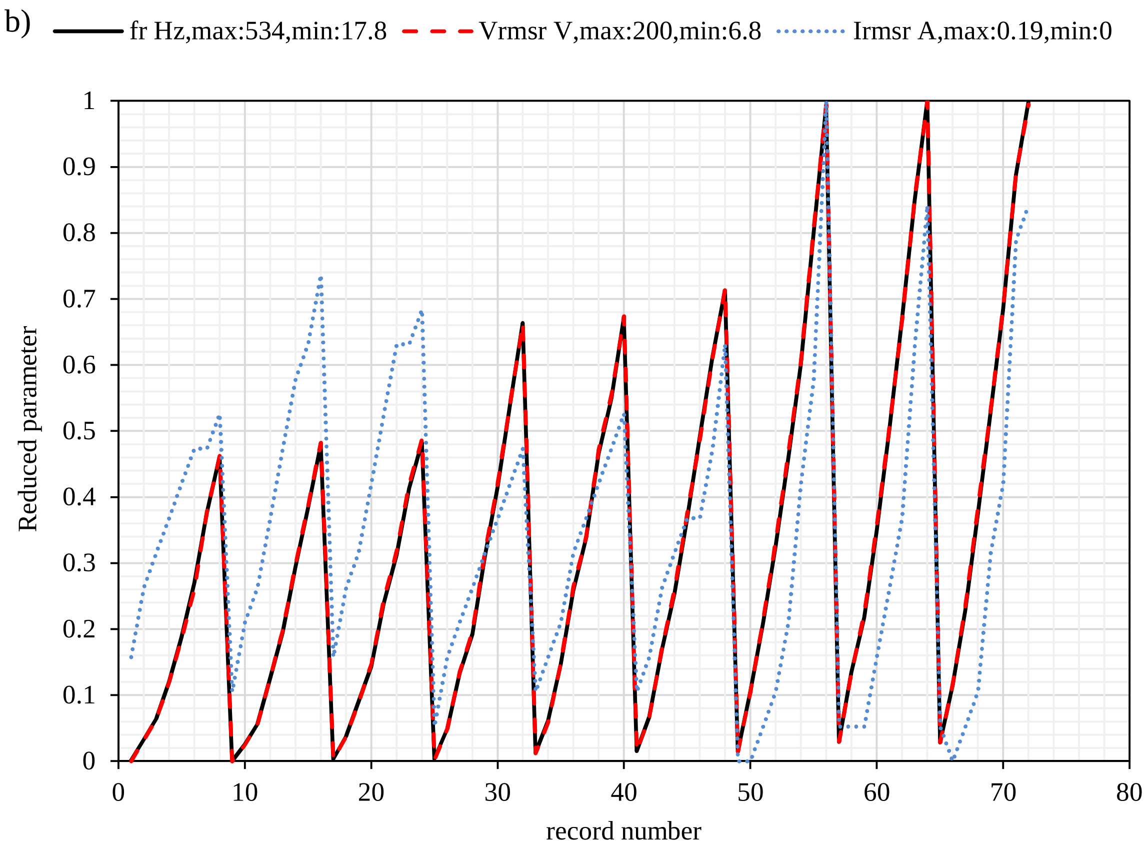

Fig. 10. Parameters of the test presented in a reduced form; a) thermodynamic parameters; b) electric parameters; *Pinr*: reduced inlet pressure, *Tinr*: reduced inlet temperature, *Qinr*: reduced inlet volume flowrate, *fr*: reduced frequency; *Vrmsr*: reduced root mean squared voltage; *Irmsr*: reduced root mean squared current.

The main experimental parameter is the inlet pressure, which is governed by the aperture of the control valve. Therefore, it is expected to rise uniformly, from the minimum to the maximum values of the inlet pressure span in each of the trials; the inlet pressure showed this consistent behaviour throughout the test.

Air is throttled from a storage tank to the inlet of the unit, and as the temperature and pressure in the tank should be kept constant, the inlet temperature is governed by the temperature in the tank. The inlet temperature is, thus, expected to mimic the behaviour of the inlet pressure and their curves should overlap in Fig. 10a. Unfortunately, unlike the pressure, the temperature at the tank is not precisely controlled because the tank is cooled with surrounding air whose temperature varied during the test. Consequently, some difference is found between the behaviour of the inlet temperature and the inlet pressure as can be observed in Fig. 10a.

The inlet volume flowrate is driven by the pressure difference from the inlet to the outlet and the hydraulic resistance across the rig. As the hydraulic resistance does not change, the volume flowrate is also expected to mimic the behaviour of the inlet pressure. As expected, a good correlation between the behaviour of the inlet volume flow rate and the inlet pressure can be seen in Fig. 10a.

Frequency is an indirect indicator of the rotational speed and therefore, readings of the frequency allowed indirectly determining the rotational speed, which simplified the setup of the experiment considerably. The rotational speed responds to changes of the inlet pressure and the load because the rotational speed is ruled by the expansion ratio and the electromagnetic brake. The frequency presented a good correlation with the inlet pressure, though a different span is identified for each of the loads. The maximum frequency is f=534Hz, which corresponds to a rotational speed ω=32,040rpm. Nevertheless, a greater frequency of f=675Hz corresponding to ω=40,500rpm was achieved but not stabilised due to intermittent operation of the air supply system under the highest air flow condition.

The root mean squared voltage is expected to have a linear correlation with the frequency in accordance with the Faraday law. As shown in Fig. 11, they have a good linear correlation whose slope corresponds to the product nBA of the generator windings, where n is the number of wire turns, B is the magnetic field and A is the area of one spire of the winding.

The root mean squared current has a complex relationship with the inlet pressure as it depends, proportionally, on the available power, and inversely on the load. This means that the current, like the frequency, is expected to mimic the behaviour of the inlet pressure but with a different span for each of the loads.

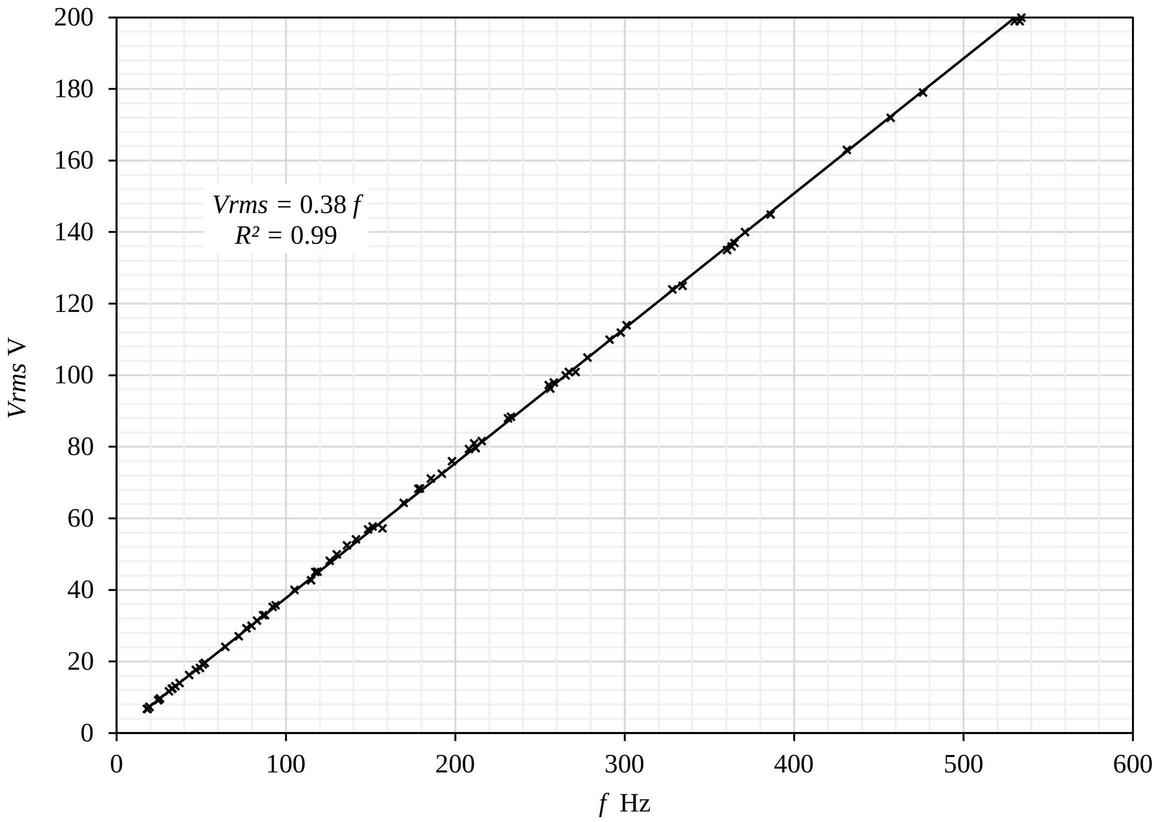

Fig. 11. Electric output of the micro-turbine-generator; *Vrms*: voltage; *f*: frequency.

The power at the load bank is calculated with the current and voltage, as described in Section 2.4. The mechanical loss is estimated and presented in Fig. 12. Although the results mimic the behaviour of the frictional moment reported in the literature of the manufacturer [39], the accuracy of this results should be experimentally confirmed for the specific application. Finally, the electrical losses are found negligible during the test as the power loss in the windings is determined to be under 0.2% of the aerodynamic power.

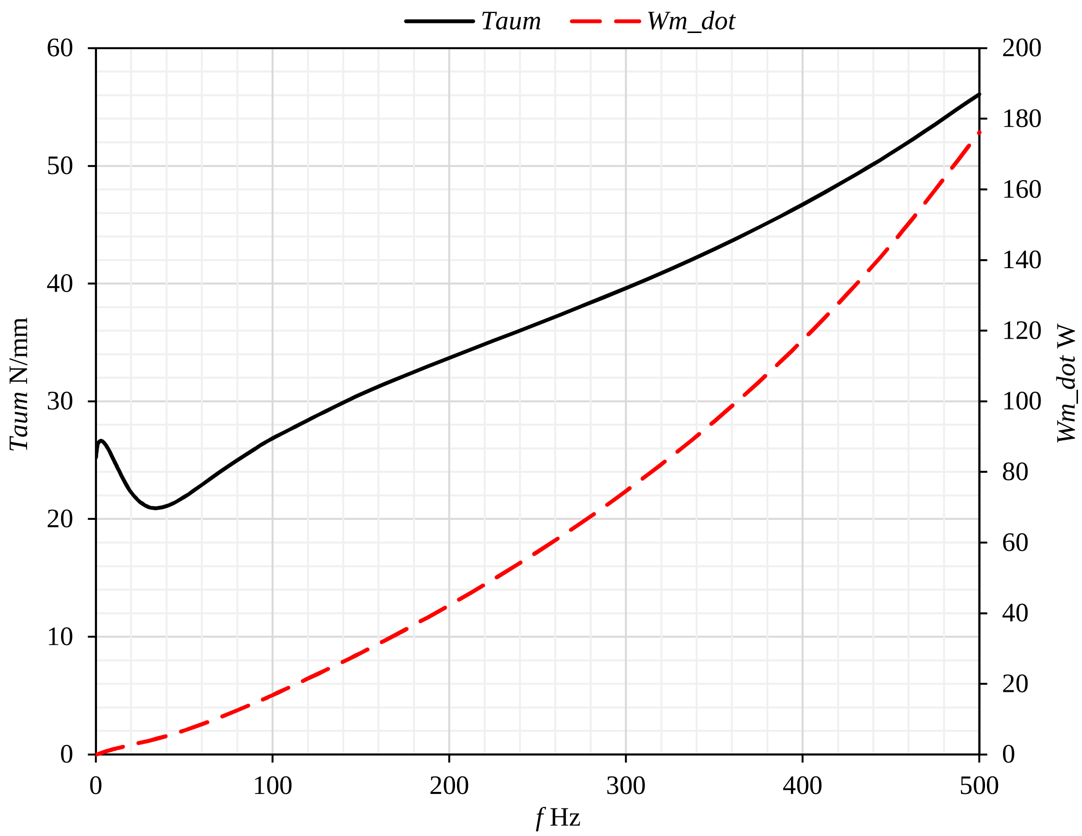

Fig. 12. Model for the estimation of mechanical loss; *f:* frequency; *Taum*: frictional moment; *Wm_dot*: mechanical power loss.

The aerodynamic efficiency obtained from the air test is compared with the aerodynamic efficiency obtained from the simulation with air, including the expected errors of both results. A comparison in the plane $\phi - \sqrt{2\psi}$ is shown in Fig. 13a, where the expected linear behaviour for an ungoverned turbine can be clearly identified. Additionally, the correlation of the simulation, with respect to the experiment, seems to be under the expected errors for a wide range of ϕ and $\sqrt{2\psi}$. In contrast, Fig. 13b and Fig. 13c show this comparison in the planes $\sqrt{2\psi} - \eta_{aero}$ and $\phi - \eta_{aero,}$ respectively. In some regions of these figures the simulation seems to have an error greater than the expected with respect to the test but, in general, both show a similar behaviour. The simulation is apparently overestimating the aerodynamic efficiency with respect to the test at high values of the flow coefficient ϕ and $\sqrt{2\psi}$ but the results have a better agreement near the point of maximum aerodynamic efficiency. This difference could suggest greater losses than those estimated in the simulation and the causes for this are diverse, however, an inaccurate estimation of the mechanical losses could be the principal reason as explained later in this section.

The comparison in the plane $BSR - \eta_{aero}$ is presented in Fig. 13d where absence of data from the test can be observed for values of BSR greater than 0.5. This situation might be caused for the lack of available fluid power during the test, which suggests the design point and hence the maximum efficiency not being achieved. The problem of deviation of experimental results with respect to simulations does not necessarily mean a wrong simulation since a deviation of results in experimental campaigns of turbines is not rare. This can be observed in the investigation performed by Kang [45], for example, where the variations of the turbine efficiency of around 0.3 are reported. However, the error might hide a systematic deviation of the simulation with respect to the test, and for that reason, further validation should be considered in future work with a reduction of sources of error.

a)

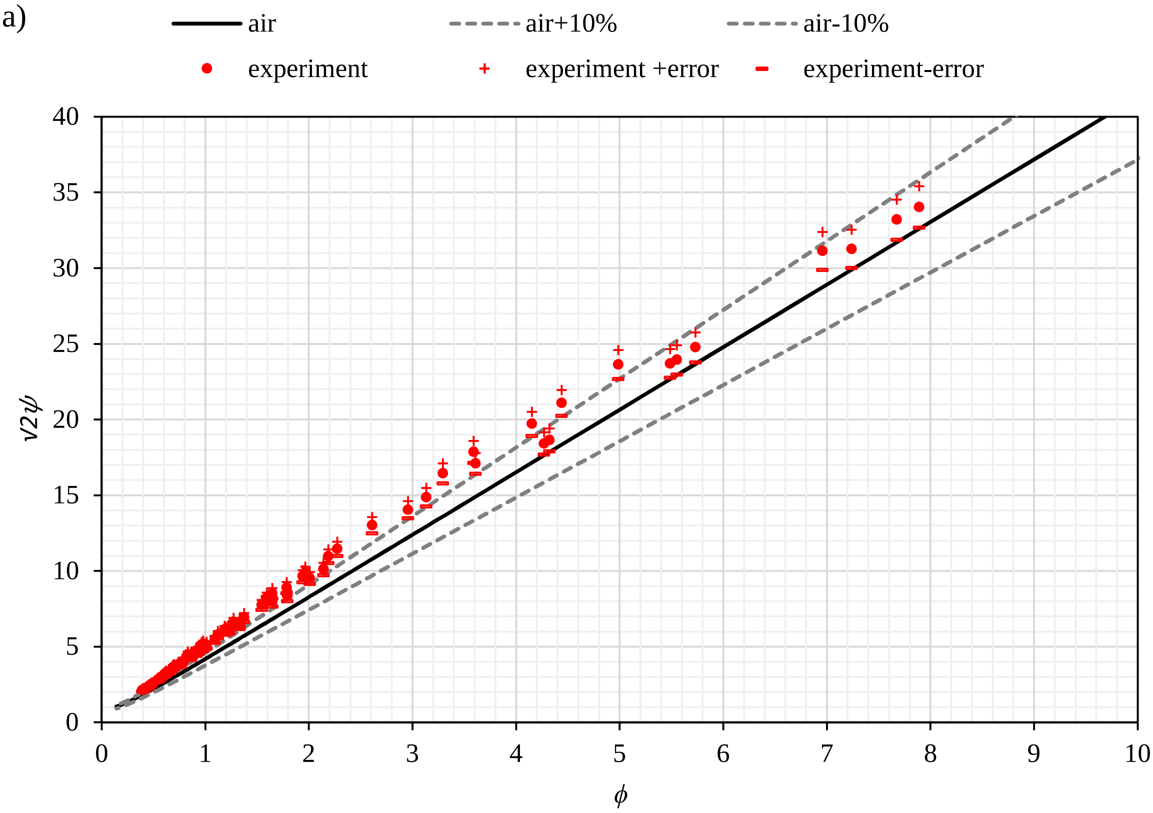

b)

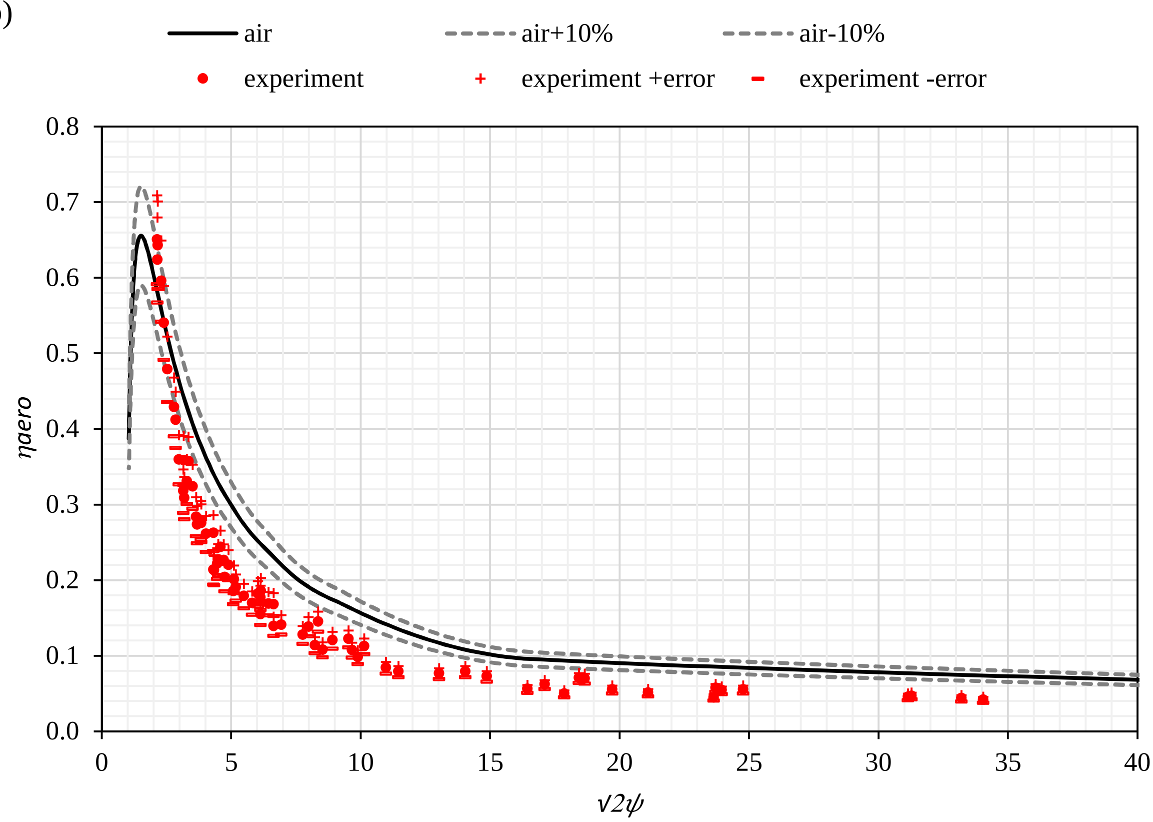
air
air+10%
air-10%
experiment
experiment +error
experiment -error
ηaero
√2ψ

c)

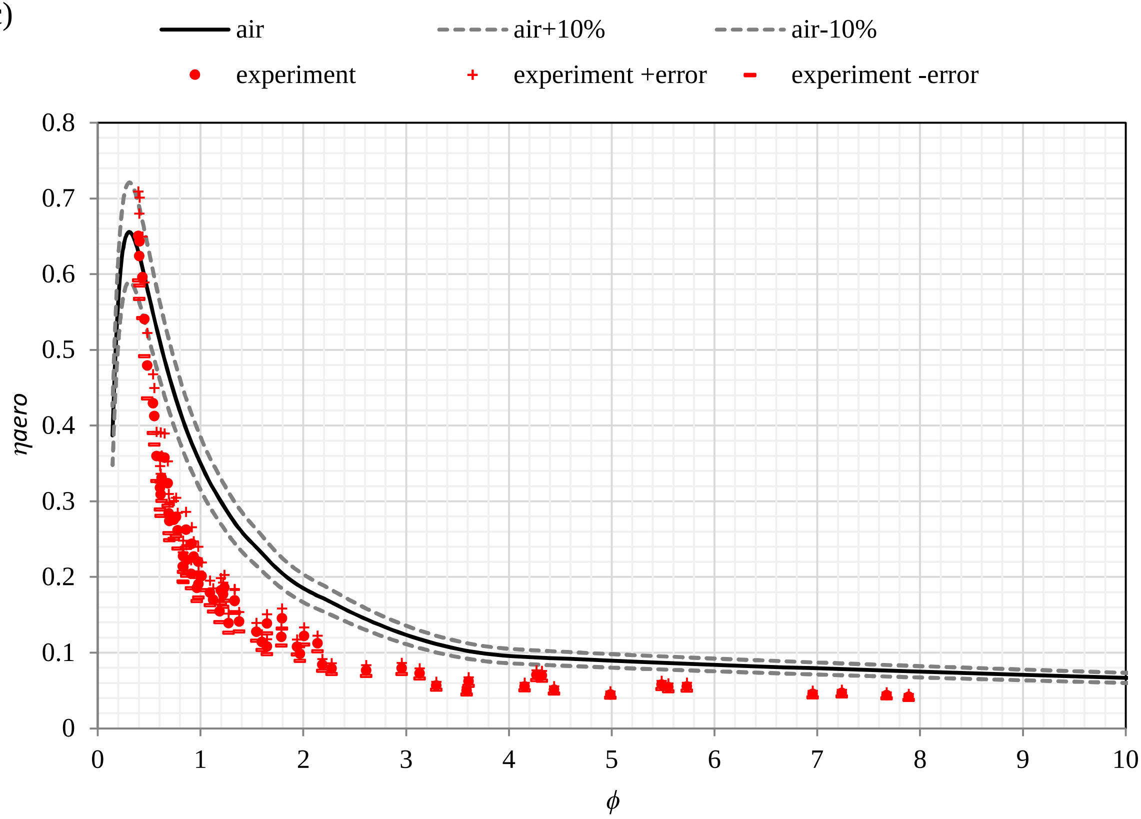
air
air+10%
air-10%
experiment
experiment +error
experiment -error
ηaero
ϕ

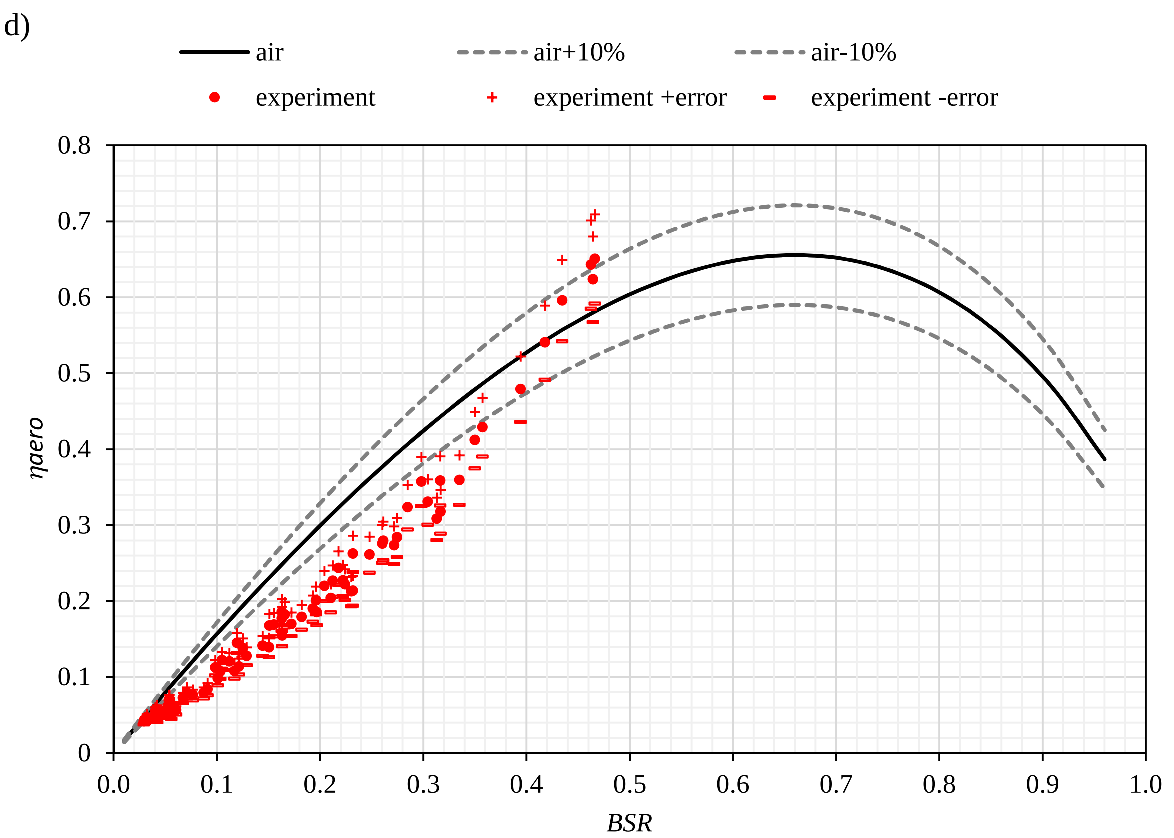

Fig. 13. Comparison of the performance between the simulation using air and the test using compressed air, including their respective ± errors; a) plane $\phi - \sqrt{2\psi}$; b) plane $\eta_{aero} - \sqrt{2\psi}$; c) plane $\phi - \eta_{aero}$ and d) plane $BSR - \eta_{aero}$; ϕ: flow coefficient, ψ: loading coefficient, *BSR*: blade speed ratio, η_{aero}: aerodynamic efficiency.

Four major sources of error are explored: inaccuracy of the estimation of the mechanical loss, imprecise fabrication of the prototype, poor control of the inlet temperature and intermittent operation of the air supply system.

The inaccuracy of the estimation of the mechanical loss may be the principal contributor to error. The mechanical loss at the bearings consumes an important fraction of the aerodynamic power, thus, inaccuracy in its determination has a major impact on the aerodynamic efficiency. Furthermore, a strong influence of the mechanical loss on the aerodynamic efficiency can be observed in *Fig. 13*d, where the lower edge of the cloud of points shows a similar behaviour with the mechanical loss shown in *Fig. 12*. This great impact of the mechanical loss on the aerodynamic efficiency could be minimised by increasing the aerodynamic power. If the micro-turbine-generator aerodynamic power is considerably greater than the mechanical loss, using a denser fluid, for example, the aerodynamic efficiency would be barely affected by mechanical loss. Moreover, if such condition is met, the rotational speed might not be limited by the lack of fluid power. This could allow the experiment to cover a greater range of blade speed ratio BSR in *Fig. 13*d and consequently, the point of maximum aerodynamic efficiency may be achieved.

An imprecise manufacturing of the prototype is a possible source of error since conventional manufacturing methods are used to simplify the fabrication of the unit. However, defects of fabrication can cause greater clearances than assumed in the simulation. With greater clearances, clearance losses could be considerably greater and consequently, the aerodynamic efficiency in the test results lower than the aerodynamic efficiency in the simulation. A solution for this could be straightforward: having strict control of clearances during fabrication and assembly. However, tighter clearances demand high precision equipment and specialised labour, which could contradict the philosophy of simplifying the fabrication of turbines of this investigation. Thus, greater clearance losses may be acknowledged in the simulation instead.

The lack of control of the inlet temperature results in the dispersion of the experimental aerodynamic efficiency. This problem is originated in the utility room where the compressor is located, which is scarcely ventilated and heats-up during operation. Although this problem could be resolved with an additional control of the temperature, a later analysis revealed that the maximum difference of the inlet temperature is 2.1K between comparable records. This difference would produce itself an error of 0.04% in the aerodynamic efficiency, 0.01% in the loading coefficient and 0.7% in the $\sqrt{2\psi}$, which is not of a major concern.

The intermittent operation of the air supply system resulted in repeated and unpredictable hydraulic transient effects. The hydraulic transience is an important source of dispersion in the experimental results as it prevents steady state readings from being reached. Two practical solutions can be implemented to reduce their impact on the experiment: the first is to replace the existing compressor with a larger flow capacity compressor and the second is to significantly increase the storage capacity of the current system. Both solutions should be considered in the future when the required resources become available.

The deviation of the simulation is not negligible with respect to the experimental results but the simulation program can still be accepted according to the reasons given below. Firstly, the simulation presents a good agreement with the design tool. Secondly, the simulation and the experimental data show a good agreement in the plane $\phi - \sqrt{2\psi}$. Thirdly, the maximum simulated aerodynamic efficiency agrees with the efficiency reported in specialised literature. Finally, the experimental results are close to the simulation near the maximum efficiency point. Therefore, the program can be used to predict the performance of the turbine using a refrigerant as the working fluid, with some deviation being acknowledged.

3.3. Prediction of the performance with a refrigerant

A prediction of the performance with a refrigerant as the working fluid can be done through simulations. However, the validation shown that in some cases the differences between the test and the simulation are greater than 10%. In these instances, the confidence in the prediction can be increased by using an equivalent prediction from a correlation with test data. Accordingly, two predictions of the performance with refrigerant as the working fluid are performed; the first based on the simulation program and the second based on the air test.

In accordance with the simulation program, the maximum aerodynamic efficiency of η_{aero}=0.66 can be achieved with a flow coefficient ϕ=0.3 and squared loading coefficient $\sqrt{2\psi}$=1.6. The micro-turbine-generator operating with R245fa in dynamic similarity should achieve identical values for those parameters. For example, for a specific enthalpy drop of Δh_{0s}=8,400J/kg proposed by Hernandez-Carrillo et.al. [25], the rotational speed would be ω=32,500rpm, the mass flowrate $\dot{m}$=0.22kg/s, the aerodynamic efficiency η_{aero}=0.66 and the aerodynamic power $\dot{W}_{aero}$=1,200W.

On the other hand, according to the test, the aerodynamic efficiency η_{aero}=0.65 corresponds to a flow coefficient ϕ=0.4 and a squared loading coefficient $\sqrt{2\psi}$=2.15. Therefore, for a specific enthalpy drop of Δh_{0s}=8,400J/kg, the unit would achieve those parameters with a rotational speed of ω=32,500rpm, a mass flow rate of $\dot{m}$=0.2kg/s and an aerodynamic power of $\dot{W}_{aero}$=1,100W.

4. FURTHER DISCUSSION

4.1. Operation capabilities

The micro-turbine-generator has proved its capability to operate in a safe manner at a high rotational speed, with a power capacity sufficient to satisfy the energy demand of an average single household. Its maximum aerodynamic efficiency is predicted to be 0.66 which is within the range of efficiency (0.35-0.8) reported by other investigations with similar capacities and applications, as reviewed by Park et.al. [46]. Therefore, the micro-turbine-generator presented in this work could be a good option of expander for domestic cogeneration systems of the ORC type. However, the prototype is yet to be tested in a real environment, i.e., using R245fa as the working fluid to confirm its capabilities in terms of reliability and performance.

The mechanical integrity of the rotor is critically governed by the centrifugal force on the blades, as exposed by Verstraete et.al. [47], hence it must be verified that the rotor withstands the required rotational speed. If this is assured, the mechanical integrity of the impeller is likely to be adequate to operate at the ORC conditions as the bending forces may not be significant. The polymeric impeller, implemented in the micro-turbine-generator, withstood rotational speeds of up to ω=40,500rpm. This is 13% above the rated rotational speed ω=36,000rpm as reported by Hernandez-Carrillo et.al. [25]. However, it is 11% lower than the maximum allowed rotational speed ω=45,720rpm defined as 127% of the rated rotational speed, based on the standard ISO10437 [48].

The datasheet of PEEK-GF30 reports a maximum service temperature of 533K but the glass transition temperature of the polyether-ether-ketone is T_g=423K according to Jean-Fulcrand et.al.; therefore, the maximum service temperature should be kept under the glass transition temperature of the polymeric matrix. The differential pressure drives the bending moment in the blades and is estimated to be lower for air than for the refrigerant. However, the bending moment does not have a critical influence on the stress of the blades, according to the analysis performed by Hernandez-Carrillo et.al. [25] and, thus, this issue should not compromise the mechanical integrity of the impeller.

From the thermodynamic, aerodynamic and mechanical perspective, the impeller should perform acceptably under the design conditions. The evidence, to this point, suggests that PEEK-GF30 can be considered a suitable candidate for replacing aluminium for the fabrication of the impeller. Nevertheless, important aspects such as the cyclic loading of the blades and the chemical interaction between the fluid and material, must be addressed before giving a final verdict.

The nozzle body, made of 3-D printed polyethylene, demonstrated to perform well whilst tested with air, and additionally, the adequate flow pattern and finishing of the surface allowed the micro-turbine-generator to achieve a state-of-the-art aerodynamic efficiency. However, the nozzle body is a static element whose principal mechanical load is the differential pressure across itself. Then, when it is exposed to an expansion of a refrigerant, the stresses in the blades may be considerably greater than the stresses experienced under an expansion of air. This issue could have a considerable influence on its mechanical performance, and consequently, a comprehensive study to examine the ability of the nozzle body to withstand the real conditions must be performed. Moreover, the unresolved issues that are identified for the impeller in terms of cyclic loading and chemical compatibility should also be addressed for the polyethylene-made nozzle body.

The generator demonstrated to perform well at high speeds. The expected voltage per phase, at the design frequency f=600Hz, is V_{rms}=224V, which is comparable with the three-phase domestic utility voltage of several countries, for example. However, as the frequency is unconventional and variable, a power converter is needed for standardising the output frequency. The maximum current is estimated to be 25% lower than the maximum allowed current of the generator windings considering the nominal application; this could reduce the electrical losses and hence the cooling needs for the generator.

4.2. Contribution to the enhancement of expanders

The replacement of metals by polymers can provide an important contribution to the improvement of ORC expanders as it impacts their technical performance and economy as explained below.

Among the technical enhancements, the reduction in weight is probably the most important as it provides lightness, an attractive feature in several elements. In the case of the impeller, for example, the implementation of a low-density material proportionally reduces the centrifugal forces in the wheel. This reduction is favourable as it enhances the mechanical integrity, promotes an agile dynamic response of the rotor and extends the lifespan of the blades. Moreover, the implementation of a low-density material reduces the imbalance due to manufacturing defects, which could make balancing less critical. A light impeller also minimises the necessity of a robust containment in the case of rotor bursting; this represents an important enhancement when compared to metallic impellers as burst containment becomes critical in domestic applications, where an enhanced safety is greatly valued.

Another attractive characteristic of polymers is the potential reduction in the production cost of parts, when compared to metal options. An example of this benefit is presented by Crawford [49], who estimated that the replacement of metals by thermoplastics in the industry of automotive parts can reduce the production cost by up to 50%. Impellers like the one used in this investigation would ordinarily be machined from a piece of metal. The fabrication process of metal impellers is typically time-consuming, labour-demanding, energy-intensive and requires the use of high-precision equipment and tools. In contrast, the production of polymeric parts by moulding is a fast process that demands minimum labour and energy per unit, which often drives an important reduction of cost in mass-production. The polymeric material itself may be more expensive compared to metal alternatives; however, the lower cost of polymeric impellers may lie with the greater savings of labour, energy and time during manufacturing. In fact, polymeric parts can be fabricated using conventional techniques that are highly economic and moreover, they give acceptable tolerances, good finishing, and short periods of fabrication. These characteristics are highly beneficial for the assurance of quality and the achievable tight tolerances may minimise the necessity of post-processing of parts, which makes the fabrication process leaner.

In fact, light, compact and easy to manufacture elements for ORC, are particularly attractive in applications where a reduced footprint and/or portability are strong requirements. The domestic cogeneration and the power conversion from waste heat of combustion engines are good examples of this, with the latter requiring portable and cost-effective ORC systems to convert waste heat to useful power.

4.3. The future of structural polymers in organic Rankine cycles

The polymeric impeller and the nozzle body of this study have shown their suitability for being implemented into a low-temperature expander. These findings may promote the adoption of polymers in other elements of expanders, e.g. casings and bearings. Furthermore, the adoption of structural polymers can be feasible for other elements of ORCs, and more generally for the refrigeration industry. The elements where polymers may be adopted include tanks, pipes, heat exchangers, pumps and valves, and beyond.

5. CONCLUSIONS

A micro-turbine-generator is designed, analysed, fabricated and tested during this investigation. The micro-turbine-generator includes a radial inflow turbine and a synchronous generator, both mounted in a common shaft. The turbine has two structural parts made of polymeric materials: the impeller and the nozzle body. The performance test of the micro-turbine-generator is conducted with compressed air as the working fluid. The main conclusions of this investigation are:

(1) The performance of micro-turbine-generator can be predicted by the developed performance simulation program with acceptable accuracy. The comparison of the results with air, ideal-R245fa and R245fa revealed a difference under 10% amongst them; therefore, a dimensionless simulation of the performance with air should reflect the aerodynamic behaviour of the unit working with R245fa.

(2) The prototype micro-turbine-generator unit has been demonstrated to work satisfactorily with air as the working fluid at off-design conditions. The impeller, machined of PEEK-GF30, responded adequately and withstood the centrifugal forces at a rotational speed of 32,040rpm and a peak rotational speed of 40,500rpm, which is a good indicator of its mechanical integrity. The 3-D printed nozzle body had an acceptable surface finishing and allowed to achieve acceptable flow angles. The generator responded as

expected providing a maximum voltage of 200V at 534Hz, however, a power converter would be required to standardise the output signal.

(3) The simulation program is validated by the compressed air test. The deviation seems to be greater than 10% in some cases, therefore, two predictions of the performance, with R245as as the working fluid, are made. The first, based on the simulation program, estimated an aerodynamic efficiency of 0.66 and an aerodynamic power of 1,200W. The second, based on the air test, showed an aerodynamic efficiency of 0.65 and an aerodynamic power of 1,100W.

The results of this study suggest that polymers may be suitable for components of expanders and other elements of ORC and refrigeration systems. However, important questions regarding their lifespan and chemical compatibility with working fluids need to be addressed in future research.

INTEREST DECLARATION AND ACKNOWLEDGMENTS

Declarations of interest: none

The authors wish to acknowledge the support provided by the technical staff of the Faculty of Engineering and The Department of Architecture and Built Environment at the University of Nottingham.

Isaias Hernandez-Carrillo wishes to express his gratitude to the Mexican Energy Ministry (SENER) and the National Council for Science and Technology (CONACYT) for financing this study through the Scholarship CONACYT-SECRETARIA DE ENERGIA- SUSTENTABILIDAD ENERGETICA 2015- ref.: 240373/409198.

NOMENCLATURE

Symbol	Description	Units
$\dot{W}$	Power	W
c_p	Heat capacity, constant pressure	kJ/kg-K
$\dot{m}$	Flowrate, mass	kg/s
A	Area	m^2
B	Field, magnetic	T
b	Blade height	m
BSR	Blade speed ratio	
c	Speed, flow absolute	m/s
D	Diameter	m
f	Frequency, electrical	Hz
FSI	Fluid Structure Interaction	-
h	Specific enthalpy	kJ/kg
I	Current, electrical	A
k	Coefficient, isentropic expansion	-
L	Length	m
n	Number of spires	-
ORC	Organic Rankine cycle	-

P	Pressure	kPa
PEEK-GF30	Polyether-ether-ketone 30% glass-reinforced	-
PETG	Polyethylene Terephthalate Glycol	-
Q	Flow rate, volume	m^3/s
R	Resistance, electrical	Ω
r	radius	m
R245fa	Pentafluoro-propane, refrigerant	-
REFPROP	Reference Fluid Thermodynamic and Transport Properties-REFPROP	-
T	Temperature	K
tc	Tip clearance	m
u	Speed, turbine blade	m/s
V	Voltage, electrical	V
Z	Number of rotor blades	-
R	Constant, ideal gas	kJ/kg-K
w	Speed, flow relative	m/s
Δh	Specific enthalpy drop	J/kg
α	Angle, absolute velocity	radian
β	Angle, relative velocity	radian
η	Efficiency (total to total)	-
ρ	Density	kg/m^3
τ	Moment, torsional	N-m
ψ	Coefficient, loading	-
ω	Speed, rotational	rpm
ϕ	Coefficient, flow	-

Subscripts	**Description**
0	Stagnation state, spouting
1	Nozzle inlet
2	Impeller inlet/nozzle outlet
3	Impeller outlet
4	Turbine exhaust
aero	Aerodynamic
bank	Load bank
c	Clearance loss, curvature
c	Corrected, curvature
cond	Condenser
e	Electrical
e	Exit loss
evap	Evaporator
f	Component in the flow direction, skin friction loss
g	Glass transition
g	Glass transition
h	hydraulic
i	Given state, iteration, incidence loss
in	Test rig inlet
loss	Aerodynamic losses
m	Mechanical
max	Maximum
min	Minimum
out	Test rig outlet
rms	Root mean square
s	Isentropic, secondary flow losses
u	Component in the blade direction
w	Winding

Superscripts	Description
‘	further
a	Phase a of generator
b	Phase b of generator
c	Phase c of generator
r	Reduced

REFERENCES

[1] International Energy Agency. Sankey Diagram. in: IEA, (Ed.).2016.

[2] R. Bracco, D. Micheli, R. Petrella, M. Reini, R. Taccani, G. Toniato. 18 - Micro-Organic Rankine Cycle systems for domestic cogeneration. in: E. Macchi, M. Astolfi, (Eds.), Organic Rankine Cycle (ORC) Power Systems. Woodhead Publishing2017. pp. 637-68.

[3] P. Balcombe, D. Rigby, A. Azapagic. Motivations and barriers associated with adopting microgeneration energy technologies in the UK. Renewable and Sustainable Energy Reviews. 22 (2013) 655-66.

[4] V.M. Nguyen, P.S. Doherty, S.B. Riffat. Development of a prototype low-temperature Rankine cycle electricity generation system. Applied Thermal Engineering. 21 (2001) 169-81.

[5] S. Quoilin, S. Declaye, B.F. Tchanche, V. Lemort. Thermo-economic optimization of waste heat recovery Organic Rankine Cycles. Applied Thermal Engineering. 31 (2011) 2885-93.

[6] G. Zywica, J. Kicinski, T.Z. Kaczmarczyk, E. Ihnatowicz, T. Turzynski, S. Bykuc. Prototype of the domestic CHP ORC system: construction and experimental research. in: V. Lemort, S. Quoilin, M. De Paepe, M. van den Broek, (Eds.), ASME-ORC2015. University of Liège and Ghent University, Brussels, Belgium, 2015. p. 9.

[7] F. Alshammari, A. Karvountzis-Kontakiotis, A. Pesyridis, M. Usman. Expander Technologies for Automotive Engine Organic Rankine Cycle Applications. Energies. 11 (2018) 1905.

[8] K. Rahbar, S. Mahmoud, R.K. Al-Dadah, N. Moazami, S.A. Mirhadizadeh. Review of organic Rankine cycle for small-scale applications. Energy Conversion and Management. 134 (2017) 135-55.

[9] G. Qiu, H. Liu, S. Riffat. Expanders for micro-CHP systems with organic Rankine cycle. Applied Thermal Engineering. 31 (2011) 3301-7.

[10] J. Bao, L. Zhao. A review of working fluid and expander selections for organic Rankine cycle. Renewable and Sustainable Energy Reviews. 24 (2013) 325-42.

[11] R. Saidur, M. Rezaei, W.K. Muzammil, M.H. Hassan, S. Paria, M. Hasanuzzaman. Technologies to recover exhaust heat from internal combustion engines. Renewable and Sustainable Energy Reviews. 16 (2012) 5649-59.

[12] Barber-Nichols Inc. Design & Manufacture of Specialty Turbomachinery. Barber-Nichols Inc.,, Arvada, CO, 2015. pp. Barber-Nichols is a proven supply chain partner that can move your prototype to production. We’re committed to quality and reliability and customers who work with us once keep coming back.

[13] Celeroton AG. Celeroton, Ultra High Speed Electrical Drive Systems. Celeroton, Volketswil Switzerland, 2008.

[14] J.E. Dyson, B.W. Darvell. Torque, power and efficiency characterization of dental air turbine handpieces. Journal of Dentistry. 27 (1999) 573-86.

[15] S. Khelladi, S. Kouidri, F. Bakir, R. Rey. Flow Study in the Impeller–Diffuser Interface of a Vaned Centrifugal Fan. Journal of Fluids Engineering. 127 (2005) 495-502.

[16] L. Shao, J. Zhu, X. Meng, X. Wei, X. Ma. Experimental study of an organic Rankine cycle system with radial inflow turbine and R123. Applied Thermal Engineering. 124 (2017) 940-7.

[17] L. Shao, X. Ma, X. Wei, Z. Hou, X. Meng. Design and experimental study of a small-sized organic Rankine cycle system under various cooling conditions. Energy. 130 (2017) 236-45.

[18] L. Li, Y.T. Ge, X. Luo, S.A. Tassou. Experimental investigations into power generation with low grade waste heat and R245fa Organic Rankine Cycles (ORCs). Applied Thermal Engineering. 115 (2017) 815-24.

[19] W. Pu, C. Yue, D. Han, W. He, X. Liu, Q. Zhang, et al. Experimental study on Organic Rankine cycle for low grade thermal energy recovery. Applied Thermal Engineering. 94 (2016) 221-7.

[20] G. Pei, J. Li, Y. Li, D. Wang, J. Ji. Construction and dynamic test of a small-scale organic rankine cycle. Energy. 36 (2011) 3215-23.

[21] W. Yagoub, P. Doherty, S.B. Riffat. Solar energy-gas driven micro-CHP system for an office building. Applied Thermal Engineering. 26 (2006) 1604-10.

[22] T. Yamamoto, T. Furuhata, N. Arai, K. Mori. Design and testing of the Organic Rankine Cycle. Energy. 26 (2001) 239-51.

[23] V. Novotný, B.B. Stunová, E. Schastlivtseva, P. Zikmund. 3D Printed Parts for Power Industry. Technological forum 2018. Czech Technical University, Prague, Czech Republic, 2018. p. 8.

[24] G. Zywica, T. Kaczmarczyk, E. Ihnatowicz, P. Baginski, A. Andrearczyk. Design and Manufacturing of Micro-Turbomachinery Components with Application of Heat Resistant Plastics. Mechanics and Mechanical Engineering. Vol. 22 (2018) 649–60.

[25] I. Hernandez-Carrillo, C.J. Wood, H. Liu. Advanced materials for the impeller in an ORC radial microturbine. Energy Procedia. 129 (2017) 1047-54.

[26] E.W. Lemmon, M.L. Huber, M.O. McLinden. NIST Standard Reference Database 23: Reference Fluid Thermodynamic and Transport Properties-REFPROP. Version 9.1 ed. National Institute of Standards and Technology, Standard Reference Data Program, Gaithersburg, 2013.

[27] K. Rahbar, S. Mahmoud, R.K. Al-Dadah, N. Moazami. Modelling and optimization of organic Rankine cycle based on a small-scale radial inflow turbine. Energy Conversion and Management. 91 (2015) 186-98.

[28] J.M. Luján, J.R. Serrano, V. Dolz, J. Sánchez. Model of the expansion process for R245fa in an Organic Rankine Cycle (ORC). Applied Thermal Engineering. 40 (2012) 248-57.

[29] H.E. Rohlik. Analytical determination of radial inflow turbine design geometry for maximum efficiency. Washington, D.C.: National Aeronautics and Space Administration

Springfield, Va.: National Aeronautics and Space Administration1968.

[30] A. Whitfield, N.C. Baines. Design of radial turbomachines, Harlow, Essex, England, 1990.

[31] J.F. Suhrmann, D. Peitsch, M. Gugau, T. Heuer, U. Tomm. Validation and Development of Loss Models for Small Size Radial Turbines. (2010) 1937-49.

[32] D. Musgrave. The prediction of design and off-design efficiency for centrifugal compressor impellers. Performance Prediction of Centrifugal Pumps and Compressors. ASME, New Orleans, 1980. pp. 185-9.

[33] C.F. Colebrook, T. Blench, H. Chatley, E.H. Essex, J.R. Finniecome, G. Lacey, et al. Correspondence. Turbulent flow in pipes, with particular reference to the transition region between the smooth and rough pipe laws. (Includes plates). Journal of the Institution of Civil Engineers. 12 (1939) 393-422.

[34] C. Rodgers, R. Geiser. Performance of a High-Efficiency Radial/Axial Turbine. Journal of Turbomachinery. 109 (1987) 151-4.

[35] A. Whitfield, F. Wallace. Study of incidence loss models in radial and mixed-flow turbomachinery. Conference on Heat and Fluid Flow in Steam and Gas Turbine Plant, Coventry, England1973. pp. 122-8.

[36] S.F. Smith. A Simple Correlation of Turbine Efficiency. The Journal of the Royal Aeronautical Society. 69 (1965) 467-70.

[37] F. Alshammari, A. Karvountzis-Kontakiotis, A. Pesiridis, P. Giannakakis. Off-design performance prediction of radial turbines operating with ideal and real working fluids. Energy Conversion and Management. 171 (2018) 1430-9.

[38] S.L. Dixon, C. Hall. Fluid Mechanics and Thermodynamics of Turbomachinery (Sixth Edition). 6 ed. Butterworth-Heinemann/Elsevier Science, Burlington, MA, 2010.

[39] SKF. The SKF model for calculating the frictional moment. in: SKF, (Ed.). pp. 1-15.

[40] M.J. Moran. Fundamentals of engineering thermodynamics / Michael J. Moran, Howard N. Shapiro. 5th ed. ed. Hoboken, N.J. : John Wiley & Sons, Hoboken, N.J., 2004.

[41] The Weather Company. Weather Underground. 2019.

[42] L. Zhang, W. Zhuge, Y. Zhang, T. Chen. Similarity Theory Based Radial Turbine Performance and Loss Mechanism Comparison between R245fa and Air for Heavy-Duty Diesel Engine Organic Rankine Cycles. Entropy. 19 (2017) 25.

[43] M. White, A.I. Sayma. The Application of Similitude Theory for the Performance Prediction of Radial Turbines Within Small-Scale Low-Temperature Organic Rankine Cycles. Journal of Engineering for Gas Turbines and Power. 137 (2015) 122605--10.

[44] M.T. White, A.I. Sayma. A Generalised Assessment of Working Fluids and Radial Turbines for Non-Recuperated Subcritical Organic Rankine Cycles. Energies. 11 (2018) 800.

[45] S.H. Kang. Design and experimental study of ORC (organic Rankine cycle) and radial turbine using R245fa working fluid. Energy. 41 (2012) 514-24.

[46] B.-S. Park, M. Usman, M. Imran, A. Pesyridis. Review of Organic Rankine Cycle experimental data trends. Energy Conversion and Management. 173 (2018) 679-91.

[47] T. Verstraete, Z. Alsalihi, R.A. Van den Braembussche. Multidisciplinary Optimization of a Radial Compressor for Microgas Turbine Applications. Journal of Turbomachinery. 132 (2010) 031004--7.

[48] I.O.f. Standardization. ISO 10437:2003. Petroleum, petrochemical and natural gas industries - Steam turbines - Special-purpose applications. International Organization for Standardization2003.

[49] M. Crawford. Metal to Plastic: Design Flexibility. in: ASME, (Ed.). ASME2013.